Title

Imaging the Breakdown and Restoration of Topological Protection in Magnetic Topological Insulator MnBi2Te4

Authors

Li, Qile
Di Bernardo, Iolanda
Maniatis, Johnathon
et al.

Publication Date

2024-02-24

DOI

10.1002/adma.202312004

Imaging the breakdown and restoration of topological protection in magnetic topological insulator $MnBi_2Te_4$

Qile Li[1,2*], Iolanda Di Bernardo[1,2], Johnathon Maniatis[1], Daniel McEwen[1,2], Amelia D.-Celorrio[1,2], Mohammad T. H. Bhuiyan[1], Mengting Zhao[1,2,3], Anton Tadich[3], Liam Watson[1,2], Benjamin Lowe[1,2], Thi-Hai-Yen Vu[1], Chi Xuan Trang[1,2], Jinwoong Hwang[4,5], Sung-Kwan Mo[4], Michael S. Fuhrer[1,2], Mark T. Edmonds[1,2,6*]

[1]School of Physics and Astronomy, Monash University, Clayton, VIC, Australia
[2]ARC Centre for Future Low Energy Electronics Technologies, Monash University, Clayton, VIC, Australia
[3]Australian Synchrotron, Clayton, VIC, Australia
[4]Advanced Light Source, Lawrence Berkeley National Laboratory, Berkeley, CA, 94720 USA
[5]Department of Physics and Institute of Quantum Convergence Technology, Kangwon National University, Chuncheon, 24341, Republic of Korea
[6]ANFF-VIC Technology Fellow, Melbourne Centre for Nanofabrication, Victorian Node of the Australian National Fabrication Facility, Clayton, VIC 3168, Australia

*Corresponding Author mark.edmonds@monash.edu and qile.li@monash.edu

Abstract –

Quantum anomalous Hall (QAH) insulators transport charge without resistance along topologically protected chiral one-dimensional edge states. Yet, in magnetic topological insulators (MTI) to date, topological protection is far from robust, with zero-magnetic field QAH effect only realised at temperatures an order of magnitude below the Néel temperature T_N, though small magnetic fields can stabilize QAH effect. Understanding why topological protection breaks down is therefore essential to realising QAH effect at higher temperatures. Here we use a scanning tunnelling microscope to directly map the size of exchange gap ($E_{g,ex}$) and its spatial fluctuation in the QAH insulator 5-layer $MnBi_2Te_4$. We observe long-range fluctuations of $E_{g,ex}$ with values ranging between 0 (gapless) and 70 meV, appearing to be

uncorrelated to individual surface point defects. We directly image the breakdown of topological protection, showing that the gapless edge state, the hallmark signature of a QAH insulator, hybridizes with extended gapless regions in the bulk. Finally, we unambiguously demonstrate that the gapless regions originate from magnetic disorder, by demonstrating that a small magnetic field restores $E_{g,ex}$ in these regions, explaining the recovery of topological protection in magnetic fields. Our results indicate that overcoming magnetic disorder is key to exploiting the unique properties of QAH insulators.

Main Text-

Topological protection has become a crucial concept in the recent development of condensed matter physics[1, 2, 3, 4]. In the quantized versions of the Hall effect (QHE), spin Hall effect (QSHE) and anomalous Hall effect (QAHE), topological protection manifests as one-dimensional electronic edge states where scattering due to local perturbations is prohibited[5]. This opens the way towards high-temperature lossless electronic transport applications[6,7] as well as new approaches to topologically-protected fault-tolerant quantum computing[8, 9]. These technologies require robust topologically protected edge channels, but in electronic devices this protection is often observed to break down. Breakdown of the QHE due to disorder, temperature, and current has been understood within scaling theory[10], and was a fundamental development in the understanding of continuous quantum phase transitions[11]. The microscopic origins of disorder-induced QHE breakdown are still a vibrant area of investigation, with new developments in graphene showing unique aspects of backscattering in the presence of both electron- and hole-like edge channels[12, 13]. The QSHE is robust to non-magnetic disorder at zero temperature[14], but magnetic disorder can cause scattering at finite temperatures[15], with a quantum phase transition from helical liquid to insulator under strong interactions[14]. In contrast, the chiral quantum anomalous Hall (QAH) edge channel supports unidirectional flow of electrical current that should be robust to any potential perturbations smaller than the exchange energy gap $E_{g,ex}$ which is opened in the surface-state of a thin film 3D topological insulator (TI) via long-range magnetic order.[16, 17] Despite this, breakdown of topological protection is ubiquitously observed at far lower temperatures than $E_{g,ex}/k_B$ or T_N, where k_B is the Boltzmann constant. In dilute magnetic doped topological insulators, this is thought to be due to magnetic disorder, leading to non-uniform magnetization and a fragile QAHE that is only observable at extremely low temperatures (<1 K).[18, 19]

Intrinsic stoichiometric magnetic topological insulators (MTIs) which possess both non-trivial topology and intrinsic magnetism, for example $MnBi_2Te_4$[20, 21] should in principle circumvent the issues associated with dilute magnetic doping. Promisingly, odd-layers of $MnBi_2Te_4$ in the 2D limit host quantum anomalous Hall states [22], leading to observation of the QAHE at 1.4 K, with the temperature increasing to 6.5 K under application of an external magnetic field[23]. Yet, this value is still substantially lower than T_N = 25 K and the activation energy extracted from transport measurements of ΔE = 0.64 meV is two orders of magnitude smaller than the predicted $E_{g,ex}$ = 70 meV (800K). Furthermore, QAHE is not routinely observed in ultra-thin odd-layer $MnBi_2Te_4$ samples or quantization is only observable in a large perpendicular magnetic field[24]. These results hint at the presence of various types of surface disorder that act to suppress the $E_{g,ex}$[25] and destroy QAHE.

To understand the mechanism of topological breakdown requires direct measurement of the interplay between surface disorder, local fluctuations in $E_{g,ex}$, and the chiral edge state with atomic-scale precision using low-temperature scanning tunneling microscopy and spectroscopy (STM/STS). A technique previously used to probe band gap fluctuations and edge states in other 2D materials[2,18,28-31]. To date, most STM/STS measurements on $MnBi_2Te_4$ have been performed on bulk crystals and have focused on point defects[26, 27, 28]. Little attention has been paid to ultra-thin films of $MnBi_2Te_4$ and the mechanisms of topological protection breakdown and suppression of QAHE. A recent report suggests connection between local magnetic Mn_{Bi}, Bi_{Mn} anti-site defects (notation X_Y means a X ion replaces a Y ion in the lattice) and collapse of the Dirac mass gap in high defect regions, but did not measure bandgap fluctuations over large areas to understand possible short-range behavior from magnetic disorder, how disorder interacts with the chiral edge state [29] or how the disorder effects respond to a magnetic field. Thus, the mechanism by which topological protection is destroyed, as well as how it recovers in *B* field, are still not understood.

In this work, we utilize magnetic field STM/STS to study the origin of QAHE suppression in 5 septuple layer (SL) $MnBi_2Te_4$. We directly measure spatial fluctuation of $E_{g,ex}$ and importantly observe the electronic overlap of the gapless edge state with gapless metallic bulk states, providing the route to breakdown of the QAHE. Finally, we demonstrate that by applying a magnetic field well below the spin-flop transition, we are able to restore the magnetic gap in the gapless regions, explaining the recovery of QAHE in small magnetic fields.

Fig. 1(a)-(b) presents the crystal structure of one septuple layer (SL) $MnBi_2Te_4$. Lattice constants, magnetic moments and possible lattice defects are labelled. Within each SL, intra-layer Mn^{2+} ions are coupled through ferromagnetic interaction. Between two adjacent SLs, two Mn^{2+} atomic layers are coupled through anti-ferromagnetic (AFM) interaction, resulting in thickness-dependent magnetic properties. We grow high-quality epitaxial ultra-thin $MnBi_2Te_4$ using molecular beam epitaxy (MBE) on Si(111)–7×7. Due to interfacial charge transfer as a result of the different work functions of *p*- and *n*-type silicon (111) the doping level in $MnBi_2Te_4$ films can be tuned. This allows for STM/STS measurements performed on $MnBi_2Te_4$ on *p*-type Si(111) with a Fermi energy that sits in the Dirac gap, whilst for ARPES measurements performed on $MnBi_2Te_4$ on *n*-type Si(111) the films are electron-doped allowing the Dirac electron band to be observed. See Methods for growth details, whilst structural characterization as well as the role of substrate and doping are found in Supplementary

Information **S1 and S2.** Supplementary **Fig. S1(b)** shows a typical large-area STM topography scan with coexisting regions of 4 and 5 SL $MnBi_2Te_4$ islands that are atomically flat, along with small pinholes of bare substrate. **Fig. 1(c)** shows a 20×20 nm atomic resolution STM image revealing the expected 1×1 atomic surface structure with lattice constant 4.3 Å. Several different defects are present; bright spots on the surface correspond to negatively charged Bi_{Te} point defects whilst the dark triangles are Mn_{Bi} defects, similar defects have been observed in Cr, Mn-doped 3D TIs[19, 30, 31] . The third defect type – Bi_{Mn} (located in the middle of each SL) is not directly visible in (c) but presented in **Supplementary Fig. S3**.

Fig. 1(d) shows an ARPES spectrum of 5 SL $MnBi_2Te_4$ thin film grown on *n*-type Si(111) taken at 8 K along ΓM direction where a Dirac cone is clearly visible near the Fermi level. The strong spectral weight near Γ in the Dirac point region could be due to Te-orbital-related matrix elements[32, 33] or be the result of bandgap fluctuations as the spectral signal is averaged over the beam spot size (100×100 μm). To demonstrate this possibility we fit the ARPES spectrum in **Fig. 1(d)** with three possible scenarios (red curve: full band gap $E_{g,ex}$ = 70 meV extracted from energy distribution curve analysis[32], green curve: reduced $E_{g,ex}$ = 45 meV, blue curve: gapless $E_{g,ex}$ = 0 meV limit).

To properly understand the $E_{g,ex}$ distribution, we use STS to measure the d*I*/d*V* spectrum (the differential conductance d*I*/d*V* as a function of sample bias *V*) which is proportional to the local density of states (LDOS) at energy $E_F + eV$, where *e* is the elementary charge. **Fig. 1(e)** shows three typical STS from the same SL terrace. The size of $E_{g,ex}$ changes drastically with location: the red STS curve corresponds to $E_{g,ex}$ = 70 meV, the green curve shows a reduced band gap $E_{g,ex}$ = 45 meV, and the blue curve is consistent with a gapless ($E_{g,ex}$ = 0 meV) spectrum (see **Fig. S4** and **Fig. S5** for details on extracting bandgap and the minimal tip-induced band bending). All spectra in **Fig. 1(e)** were taken more than 5 nm away from step edges in order to exclude effects from edge states.

Before turning to the origin of the band gap variations, we probe the step edge between 4 and 5 SL $MnBi_2Te_4$, to verify the presence of the conductive edge state, a consequence of topological protection and signature of a QAHI. In principle, the edge state exists at the edge of the sample where the height profile on the sample drops from 5SL thickness to the underlying substrate. However, due to a variety of growth and measurement practicalities, measuring the edge state on the sample edge with STM is extremely challenging. Therefore, instead we probe the edge state on the 5SL (Chern number of ± 1) to 4SL (Chern number of 0) step edge enabled by the unique thickness-dependent topological property of $MnBi_2Te_4$.[22] Since the edge state appears on the boundary between two phases with different topological invariant, the physics of the edge state on the terrace edge is equivalent to that of the edge state on the sample edge.

Figure 2(a) and **(b)** show STM topography and d*I*/d*V* maps taken across two different 4 to 5 SL step edges on two separately grown $MnBi_2Te_4$ thin films. Since the chiral edge state exists within the Dirac band gap, the sample bias was tuned into the Dirac band gap to image the edge state. The lower panel of **Fig. 2(a)** shows a d*I*/d*V* map taken at +25 mV: a pronounced increase in d*I*/d*V* signal is observed that is localized at the step edge (which is marked by a red dashed line), indicating a conductive edge state. This conductive edge state is mostly continuous, but has strong hybridization between the edge state and disordered bulk states and not spatially isolated. The second edge presented in **Fig. 2(b)** shows another step edge consisting a 5SL edge (orange arrow) and sub-step edge (excluded in the figure). The sub-step edge structure has also been observed in previous STM study on $MnBi_2Te_4$ thin films[29]. The middle and lower panel of **Fig. 2(b)** show d*I*/d*V* maps taken at 0 and -15 mV: that also show a pronounced increase in d*I*/d*V* signal that is localized at the step edge. At bias outside the Dirac gap (-15 mV), this edge state is weakly coupled to bulk state with finite spectral weight between the edge channel and the gapless bulk states. As the bias moves into the Dirac gap (0 mV), the edge states become spatially isolated unlike the edge state presented in **Fig. 2(a)**. We have included more d*I*/d*V* maps at other voltage bias, see **Fig.S6** to demonstrate the decoupled edge channel in the Dirac gap. We must point out the spectral intensity along the edge in **Fig. 2(b)** seems to be disconnected, which has been also observed in previous reports on topological edge states of $MnBi_2Te_4$[34], its related heterostructure with Bi_2Te_3[35], as well as the 2D topological insulator WTe_2[36]and may arise due to local roughness and structural disorder along the edge. Furthermore, we have also performed a similar d*I*/d*V* map on a 4SL to 3SL edge, and no spectral intensity is observed (**Fig.S7**), indicating the 1D edge state could be only present on odd-layer SL $MnBi_2Te_4$that is buried underneath the step edge and is very difficult to probe from the surface. For a perfect QAHI there should be a well-defined suppression of the bulk LDOS within the bandgap, but we observe bulk regions well away from the edge that also show strong LDOS at the same energy, indicating the coupling between edge state and disordered bulk metallic regions. To confirm that some disordered bulk regions are indeed metallic, in **Fig. 2(c)** we measure d*I*/d*V* spectra corresponding to the edge state (red curve) at point A, normal bulk states (purple curve) at point B, and disordered bulk states (black curve) at point C, D in **Fig. 2(b)**. The normal bulk region right next to the edge shows the expected insulating behavior with $E_{g,ex}$= 40 meV, but the d*I*/d*V* spectra at both the edge and within these disordered bulk state regions are quite different, with states filling the entire bulk gap. The disordered bulk states have much stronger spectral intensity above zero bias in the conduction band range and the STS curves resembles the DOS of a gapless Dirac cone[37]. This indicates a continuous metallic percolative path for electron transport from the edges through the bulk. **Figure 2(d), (e)** shows spatial d*I*/d*V* profiles as a function of distance away from the edge measured along the two green lines in **Fig. 2(b)** (labelled as Cut 1 and Cut 2) that demonstrate the extended nature of the edge state feature along the step edge located at 5 nm, as marked by the red arrow. The other spectral intensity between 0 to 2 nm is clearly separated from the edge state, and we assign it to the disordered bulk states, marked by a white arrow. **Figure 2(f)** shows the summed d*I*/d*V* intensity (red curve extracted from **Fig. 2(d)**; green curve extracted from **Fig. 2(e)**) within the bulk Dirac gap. Moving away from the edge shows the expected exponential decay for a 1D topologically non-trivial edge state.[2,38] The extracted exponential decay lengths are 0.82 ± 0.38 nm and 1.22 ± 0.41 nm. Although the observed edge state appears to be isolated from the metallic bulk states, the small spatial separation (less than 3 nm) implies fragile edge state conduction. The observation of a 1D edge state on two different step edges (**Fig. 2** and additional data presented in **Fig. S8**), suggests the 1D edge state exists on the 5SL to 4SL edge, independent of the exact edge structure and evidence of a QAH gapless edge state. However, the presence of both disordered bulk state and edge state on the 5SL terrace suggests that the edge state hybridizes with the metallic regions formed by these disordered bulk states, and these metallic regions represent continuous conductive pathways that guide the edge state into the bulk, leading to the conductive breakdown of QAHE through dissipative bulk conduction and resulting in non-perfect quantization of Hall conductance and non-zero longitudinal resistance.

To investigate the origin of these metallic regions formed by disordered bulk states, we perform atomic resolution topography and STS maps around the magnetic defects Mn_{Bi} and Bi_{Mn}, which allow us to extract maps of the spatial variation of $E_{g,ex}$, and the gap center energy E_c to determine the influence each defect has on the electronic structure. E_c is equivalent to extrapolating the massive Dirac bands linearly into the gap to obtain the Dirac point in the gapless limit. At locations where the Dirac bands are gapped, E_c is a good measure of local doping shifts associated to the magnetic order. Bi_{Te} defects, are non-magnetic, thus, are unlikely to result in fluctuations in the exchange energy gap $E_{g,ex}$. **Figure 3(a)** illustrates the position of a Mn_{Bi} defect in the crystal lattice, and **Fig. 3(b)** shows an atomic resolution image of 10×5 nm area (-500 mV, 3 nA) with Mn_{Bi} defects marked in black triangles. The Mn_{Bi} defect density can be estimated to be around 6%, which is very similar to the defect concentration reported in previous study on MBE grown $MnBi_2Te_4$ film[29] but is almost double the concentration observed on the surface of a cleaved bulk $MnBi_2Te_4$ crystal [27]. The substitution of Bi^{3+} by Mn^{2+} causes contraction on the three neighboring surface Te atoms[27]. **Fig. 3(c)-(d)** are maps of $E_{g,ex}$ and E_c extracted from the dI/dV spectra on the same area in **(b)** (details found in **Supplementary Fig. S4**).

Representative dI/dV curves from different locations, marked with $E_{g,ex}$ and E_c values, are plotted in **Supplementary Fig. S9**. The Mn_{Bi} defects on the surface (green triangles) are barely visible in the maps of $E_{g,ex}$ and E_c in **(c)** and **(d)** respectively, with only small local decrease in $E_{g,ex}$ and slight increase in n-type doping (due to the negative charge of the Mn_{Bi} defects) observed. Instead, the fluctuations in $E_{g,ex}$ and E_c appear to be correlated, and to be spatially coherent over length scales of at least a few nanometers, i.e. larger than a single defect which is about 0.5 nm. Gap size histograms of Mn_{Bi} regions and Mn_{Bi} excluded regions are shown in **Fig. 3(e)**. In regions without Mn_{Bi} defects, the $E_{g,ex}$ histogram is skewed towards larger gap size when compared to regions with Mn_{Bi} defects, which can be explained by effectively reduced exchange coupling between surface state and magnetic moments due to the AFM interaction between the Mn_{Bi} defects and Mn^{2+} ions. Overall, the patterns of gapped and gapless regions formed over several nanometers are very different from the band gap fluctuations in dilute magnetic doped TIs[19,31]. In dilute magnetic doped TIs, the random distribution of antisites formed by magnetic 3d transition metal ions is directly responsible for the fluctuation. But in the current case of 5SL $MnBi_2Te_4$ thin film, the observed pattern in the $E_{g,ex}$ map appears to be not correlated to distribution of Mn_{Bi} defects, suggesting additional major contribution from magnetic disorder to the gap fluctuations. The origin of the magnetic disorder can be complicated but is very likely to be defect driven. The local deficiency of Bi p-states on Mn_{Bi} defects could indirectly modulate the weakened intralayer ferromagnetic interaction among Mn^{2+} magnetic moments through non- negligible p-d interactions, as reported by recent magneto-optics and inelastic neutron scattering studies[39,40]. In **Fig. 3(f)**, a Bi_{Mn} defect in the middle atomic layer is depicted, where the substitution results in the absence of magnetic moment. Such defects manifest as large bright triangles and are only visible at positive bias as marked by purple triangles in **(g)**. The three bright dots in each triangle are due to Te p-orbitals on the surface responding to Bi_{Mn} defects[27]. dI/dV mapping was performed in the area marked by the yellow box in **(g),** with the band gap and gap center maps shown in **Fig. 3(h)-(i)**. The band gap map in **(h)** and the histogram in **(j)** show that the substitution of magnetic Mn^{2+} ions at

Bi_{Mn} defects renders the local lattice site non-magnetic, thus, gapless regions. However, regions well away from the Bi_{Mn} defect still display band gap fluctuation with significant weight of gapless states, suggesting that Bi_{Mn} defects alone do not result in extended regions of suppressed Dirac band gap and metallicity in the bulk. The results in **Fig. 3** therefore demonstrate the band gap and gap center fluctuations cannot be explained entirely by local gap suppression by any of the three types of isolated point defects discussed above and imply the possibility that longer-ranged collective behavior of magnetic disorder is responsible for the extended Dirac band gap suppression on the surface of $MnBi_2Te_4$.

To understand the origin of the observed large-scale band gap fluctuations, we measure STS mapping with and without magnetic field to examine how the extended gapless structures respond to $B_\perp$ field. **Figure 4(a)** shows STM topography of the atomically flat scan region at $B_\perp$=0 T**.** (See **Fig.S10** for the topography scan taken at 0T and 1T where the map region has been carefully aligned using the defects). In **Fig. 4(b)** STS curves taken at different locations show three types of behavior: gapless regions (blue), gapped regions with fluctuating Dirac band gap (green and red) and regions where the Dirac electron band is suppressed and manifests as an anomalously large bulk gap (orange). Such conduction band (CB) suppression has been previously observed in bulk $MnBi_2Te_4$[27]. The diminished CB intensity prevents us from extracting accurate values of $E_{g,ex}$, thus, the CB suppressed regions are masked in black in the following gap maps and excluded in subsequent analysis. The CB suppressed regions are identified by summing the STS intensity above +20 mV bias at each point and comparing to a summed threshold value of 1.28×10^{-11} for 0 T map and 1.85×10^{-11} for 1T map that are estimated from STS curves with weak CB intensity and optimized. **Figure 4(d)** plots STS curves taken at the same location (green circle in **(a)**) that is initially gapless at $B_\perp$=0 T (blue curve) and $B_\perp$=1 T (red curve). It is immediately clear that a 1 T field is sufficient to restore $E_{g,ex}$ to 40 meV with enhanced exchange coupling. Having observed magnetic field induced band gap modulation, we now perform d*I*/d*V* mapping (-150 mV, 0.4 nA) on an 80×80 point-mesh on the same 30× 30 nm area in **(a)** at $B_{\perp}$=0 T (**Fig. 4(c)**) and $B_{\perp}$ =1 T (**Fig. 4(e)**). Histograms of $E_{g,ex}$ with and without B field are shown in **Fig. 4(f)**. These maps reflect the spatial fluctuation of $E_{g,ex}$ over larger scale and will be used to investigate its origin beyond point defects. The histogram in the upper panel of **Fig. 4(f)**, shows prominent weighting for $E_{g,ex}$ < 10 meV, corresponding to a skewed normal distribution (skewness 0.91) with mean of 26.3 meV and standard deviation of 25.8 meV. Upon applying $B_{\perp}$=1 T, the histogram in the lower panel of **Fig. 4(f)** shows a significant reduction in $E_{g,ex}$ < 10 meV regions, and a gap opening and renormalization that results in a near-normal distribution (skewness 0.06) with an increased mean of 44.3 meV and smaller standard deviation of 20.2 meV. A statistical analysis of regions that possess unsuppressed CB intensity at both 0T and 1T is presented in the Supplementary Information in **Fig. S11**. This shows the average band gap increases by 20.6 meV to a value of 37.8 meV in the 1T magnetic field and more bimodal distribution. Additionally, to reveal the gradual change of the $E_{g,ex}$ in low to medium magnetic field, we have performed magnetic field dependent mapping between 0 and 0.8 T on a different sample, see **Fig. S12** where the majority of gap renormalization occurs at 0.8 T.

We now consider possible origins of the extended suppressed gap structures. As recently observed in magnetic force microscopy measurements[41], whilst the bulk of $MnBi_2Te_4$ thin film remains AFM coupled, the surface exhibits magnetic spin flops which could be enhanced by Bi_{Mn} defects or changes to the size of the inter-layer van der Waals gap near the surface[42]. In our thin film $MnBi_2Te_4$ samples, we are able to align the magnetic moments at $B_{\perp}$=1 T, much lower than required for inducing surface (2-3.5 T) and bulk spin flop (7.7 T) in previous work[41,43,44], which indicates that surface spin flop has negligible contribution to the exchange gap fluctuation observed. This suggests that there is significant magnetic disorder most likely in the first SL, a magnetic uncompensated layer, that causes band gap fluctuation on the nanometer scale[25]. Such magnetic disorder occurs in the Mn^{2+} layer located at the center of the top SLs, which is very hard to probe using STM. However, the exchange interaction of the Dirac states with Mn^{2+} ions enables indirect mapping of such magnetic disorder based on the suppression of $E_{g,ex}$ as seen in **Fig. 4(c)** and **(e)**.

Fig. 4(g) illustrates the situation schematically. Magnetic disorder causes local suppression of the exchange gap (blue gapless Dirac spectrum) in extended regions due to long-range exchange interactions among local moments, while some regions retain partial (green band structure) or full (red band structure) gaps. Application of $B_{\perp}$=1T (bottom) aligns the moments of magnetically disordered regions, increasing the gap (red band structure). Interestingly, the *B* field also decreases the area of suppressed CB regions, suggesting CB suppression is also related to disordered magnetic moments beyond the influence of deficient Bi orbitals due to Mn_{Bi} defects[27]. Finally, we propose an explanation to the origin of the magnetic disorder. The prevalent band gap fluctuation observed implies weakened inter-layer and intra-layer exchange interaction in 5 SL $MnBi_2Te_4$. Its low magnetic anisotropy energy makes $MnBi_2Te_4$ similar to a 2D Heisenberg magnet that does not sustain long-range ferromagnetic order[40, 44, 45]. Such weakened magnetic anisotropy makes the magnetic ordering more vulnerable to magnetic defects, especially Bi_{Mn}. With Mn^{2+} ions replaced by non-magnetic Bi^{3+} ions, exchange coupling between intra-layer Mn^{2+} ions is weakened, depending on the concentration of such defects. Although, the direct exchange coupling between Mn_{Bi} and surface states is much weaker as discussed in **Fig. 3**, Mn_{Bi} can still cause local deficiency of Bi *p*-orbitals and indirectly influence the magnetic moments in the middle of SL by *p-d* interaction. Therefore, the ferromagnetic configuration of Mn^{2+} ions could be canted and disordered in the presence of a large amount of anti-sites defects, resulting in reduced magnetization and gapless spectra over extended areas. Similar mechanism has also been reported recently[29]. Lastly, we present an $E_{g,ex}$ map of a region with larger amount of Bi_{Mn} defects in 0 T and 1 T magnetic field in **Fig. S13.** This region is indeed mostly gapless. Upon applying the 1T field, a significant reduction of gapless regions occurs (further details in **Supplementary Fig. S13**).

CB suppression is almost absent in this region, which can be explained by the large amount of Bi_{Mn} defects that offers sufficient *p*-states to form Dirac bands.

Using magnetic field STM/STS measurements, we have demonstrated that the gapless edge state in QAHI 5 SL $MnBi_2Te_4$ is directly coupled to extended percolating bulk metallic regions arising from band gap fluctuations caused by magnetic surface disorder. By applying a magnetic field, the band gap fluctuations can be greatly reduced, and the average exchange gap increased to 44 meV, close to predicted values for 5 SL $MnBi_2Te_4$ [21,22,32]. These results provide insight on the mechanism of topological breakdown and how it can be restored in a magnetic field[23,24]. Minimizing magnetic disorder will be the key to realizing QAHE in not only odd-layer $MnBi_2Te_4$ ultra-thin films but also other MTIs at elevated temperature in the future. The weak interlayer interaction and intralayer ferromagnetic ground state close to instability limit in $MnBi_2Te_4$ makes it difficult to sustain long-range magnetic order especially with significant amount of anti-site defects, and improved $MnBi_2Te_4$ crystal or film growth alone may not be sufficient to fully mitigate magnetic disorder. Therefore, other strategies such as heterostructure engineering $MnBi_2Te_4$ with other robust, highly anisotropic 2D ferromagnets [46] or ferromagnetic/topological insulators sandwich heterostructures [47,48,49] may be required to achieve the robust topological protection required for next-generation lossless electronics and topological quantum computing[6,7,8,9].

Methods

Growth of Ultra-thin $MnBi_2Te_4$ on Si(111)

Ultra-thin $MnBi_2Te_4$ thin films were grown in a Scienta Omicron Lab 10 molecular beam epitaxy (MBE) growth chamber. The Si(111) substrate was flash-annealed at 1180°C with direct current heating to achieve an atomically flat (7×7) surface reconstruction. Effusion cells were used to evaporate elemental Mn (99.9%), Bi (99.999%) and Te (99.95%). A quartz crystal microbalance was used to calibrate rates before growth and reflection high-energy electron diffraction (RHEED) was used to monitor the crystal growth in-situ. Each SL of $MnBi_2Te_4$ was grown by first growing 1 quintuple-layer Bi_2Te_3 followed by growing a bilayer MnTe in overflux of Te at 230 °C. 1 SL $MnBi_2Te_4$ forms spontaneously by re-arranging MnTe layer into the middle of 1QL Bi_2Te_3 similar to $MnBi_2Se_4$[50]. The growth time for each 1QL Bi_2Te_3 and MnTe was calibrated from the oscillation of the RHEED pattern. Then the process was repeated five times to reach the desired thickness and finished with a post-annealing process in Te flux for 10 min to improve crystallinity. The films were subsequently capped with 10nm amorphous Te, to allow transfer in air to the STM chamber.

Scanning Tunneling Microscopy/Spectroscopy (STM/STS) Measurements

The capped films grown on boron doped silicon (111) (resistivity 0.1-0.2 $\Omega \cdot$ cm) were transferred in air to a Createc LT-STM chamber and were annealed in UHV at 290°C for 2.5 hours to remove the Te capping before performing STM measurements at 4.3 K. A PtIr tip was prepared and calibrated using an Au (111) single crystal, confirming the presence of the Shockley surface state at -0.5 V and flat LDOS near the Fermi level before all measurements. The STM differential conductance measurements (d*I*/d*V*) were performed using standard lock-in method with 5 mV AC excitation voltage at 797Hz for Dirac gap mapping and 2mV AC excitation voltage at 797Hz for edge state mapping. Differential conductance measurements were made under open feedback conditions with the tip in a fixed position above the surface. For the magnetic field dependent STM/STS measurements, a magnetic field up to 1T was applied perpendicular to the sample.

Angle-resolved Photoemission Spectroscopy (ARPES) Measurements

ARPES measurements were performed at Beamline 10.0.1 at Advanced Light Source (ALS) in Lawrence Berkeley National Laboratory, USA. A 5 SL $MnBi_2Te_4$ sample was grown on antimony doped silicon (111) substrate (resistivity 0.1-0.2 $\Omega \cdot$ cm) following the same growth procedure in an MBE system integrated with the beamline endstation and transferred into the measurement chamber after growth. Data was taken using a Scienta R4000 analyser at 8K and photon energy of 50 eV was selected to optimize the signal. The combined energy resolution is 15-20 meV and the angular resolution is 0.2°, or equivalent to 0.01Å^{-1} momentum resolution for the photon energy used.

Acknowledgements

M. T. E., Q. L., M. S. F., I. D. B. acknowledge funding support from ARC Centre for Future Low Energy Electronics Technologies (FLEET) CE170100039. Q. Li acknowledges funding support from the AINSE postgraduate award. This research used resources of the Advanced Light Source, which is a DOE Office and Science User Facility under contract no. DE-AC02-05CH11231. M.T.E. and Q.L. acknowledge travel funding provided by the International Synchrotron Access Program (ISAP) managed by the Australian Synchrotron, part of ANSTO, and funded by the Australian Government. This work was performed in part at the Melbourne Centre for Nanofabrication (MCN), the Victorian Node of the Australian National Fabrication Facility (ANFF).

Author contributions

M. T. E and Q. L. devised the STM experiments. Q. L. performed the MBE growth and STM/STS measurements at Monash University. I. D. B., B. L., L. W. and T.H.Y.V assisted the scanning probe measurements. J. H., S.-K. M. and C. X. T assisted the ARPES measurements. Q. L. performed data analysis with assistance from M. T. E, M. S. F, J. M and D. M. Q. Li, and M. T. E. composed the manuscript. All authors read and contributed feedback to the manuscript.

Data availability

All raw and derived data used to support the findings of this work are available from the authors on reasonable request.

FIGURES

FIGURE 1

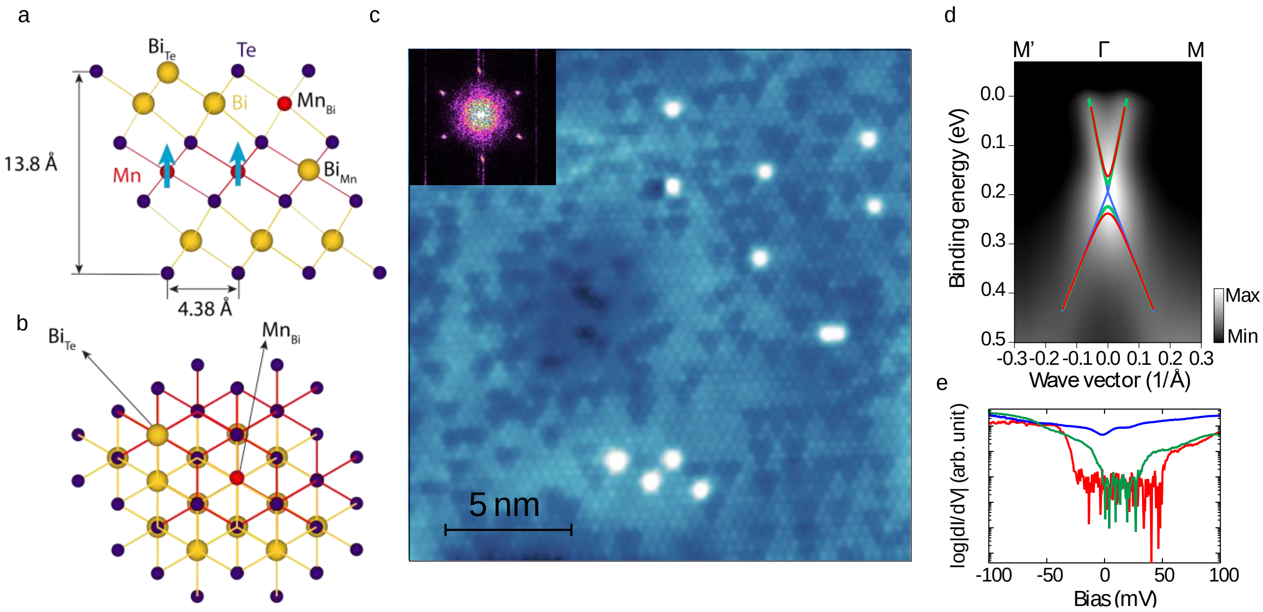

Figure 1 | Characterization of epitaxial ultra-thin $MnBi_2Te_4$ and overall electronic structure from ARPES. **a, b** Crystal structures of a septuple layer of $MnBi_2Te_4$. **(a)** side view of the lattice with lattice constants, atom species, and defects labelled. The magnetic moments on Mn^{2+} ions are marked with blue arrows. **(b)** Top view of the lattice. **(c)** Atomic resolution image (-2 V, 180 pA) of a flat 20×20 nm area where Mn_{Bi} (dark triangles) and Bi_{Te} (bright dots) defects are clearly visible. The insert shows the fast Fourier transformed image of the same area. (Note the spots corresponding to 1×1 surface atomic structure). **(d)** Angle-resolved photoemission spectrum of five-layer $MnBi_2Te_4$ along Γ-M where the fully gapped ($E_{g,ex}$ = 70 meV) band dispersion is marked by red curve. Green and blue are illustrations of possible reduced gap and gapless dispersions ($E_{g,ex}$ = 35 meV and 0 meV respectively). **(e)** d*I*/d*V* spectra taken at different locations on the same terrace of 5 SL $MnBi_2Te_4$ (-0.2 V, 400 pA) showing gapless (blue curve), reduced gap (green curve) and fully gapped d*I*/d*V* curves from different regions on the same terrace.

FIGURE 2

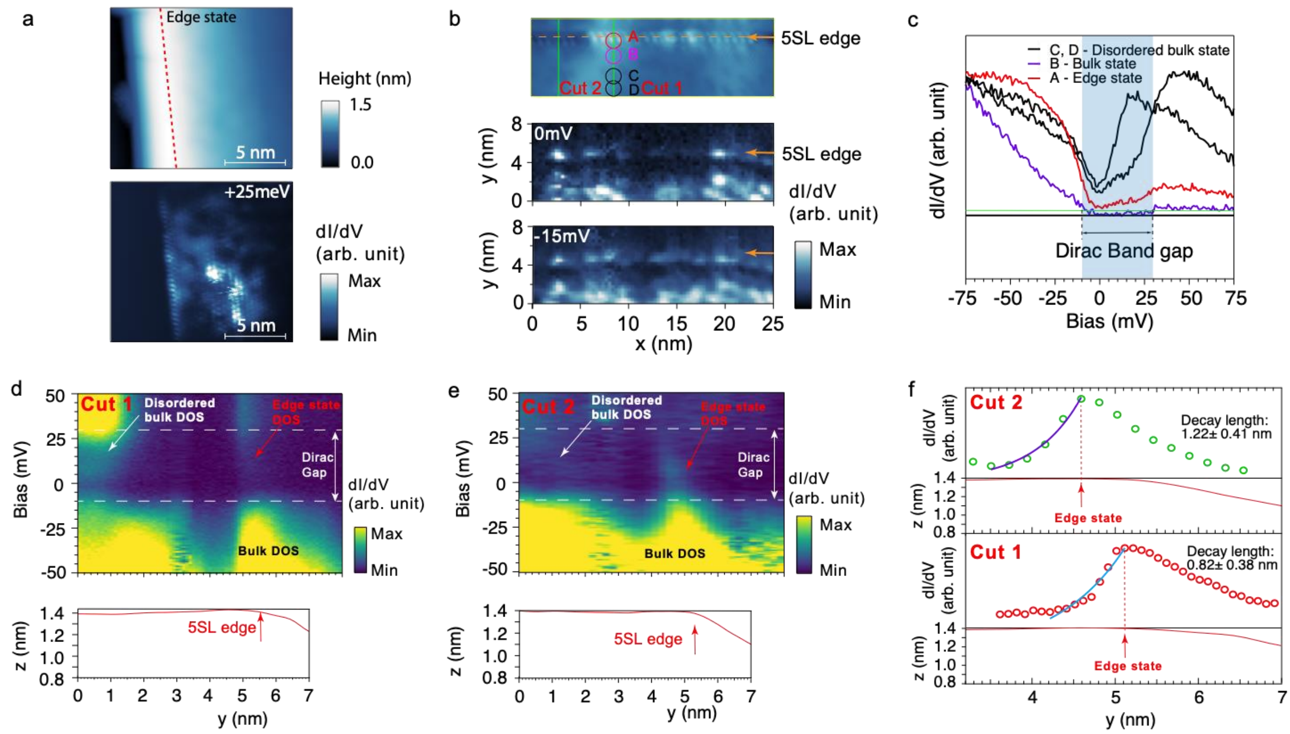

Figure 2 | Visualizing the gapless edge state and its coupling to bulk metallic states. (a)-(b) STM topography taken at -1V (upper panels) and d*I*/d*V* maps (lower panels) taken across two different 4 to 5 SL $MnBi_2Te_4$ step edges. **(a)** d*I*/d*V* map at +25 mV bias (40 pA) shows a pronounced increase in intensity at the edge state and its strong coupling to bulk metallic states. The location of the edge state is marked by a red dashed line. **(b)** d*I*/d*V* maps (-0.15V, 400pA) at 0 mV and -15 mV bias show the spatial distribution of the edge state taken across a step edge and how the edge state is isolated from the bulk metallic states. The positions of the 5SL edge is marked with orange arrows. **(c)** d*I*/d*V* spectra (-0.15V, 400pA) taken from edge state region A (red circle), disordered bulk region C, D (black circle) and normal bulk region B (purple circle) as marked in **(b)**. **(d)**,**(e)** d*I*/d*V* spectra (-0.15V, 400pA) and height profile taken across the edge from paths marked by green lines in **(b)**. The horizontal axis of the spectra is aligned with the height profile. The edge state is marked by red arrow and other in-gap peaks are attributed to disordered bulk states which is marked by white arrows. The white horizontal dashed line shows the range of Dirac gap which is the same as the shaded region in **(c)**. **(f)** d*I*/d*V* intensity averaged in the Dirac gap and plotted as a function of distance in y direction showing exponential decay. The height profiles of the two cuts are shown below the d*I*/d*V* profiles respectively where the intensity maximum of the edge state is marked.

FIGURE 3

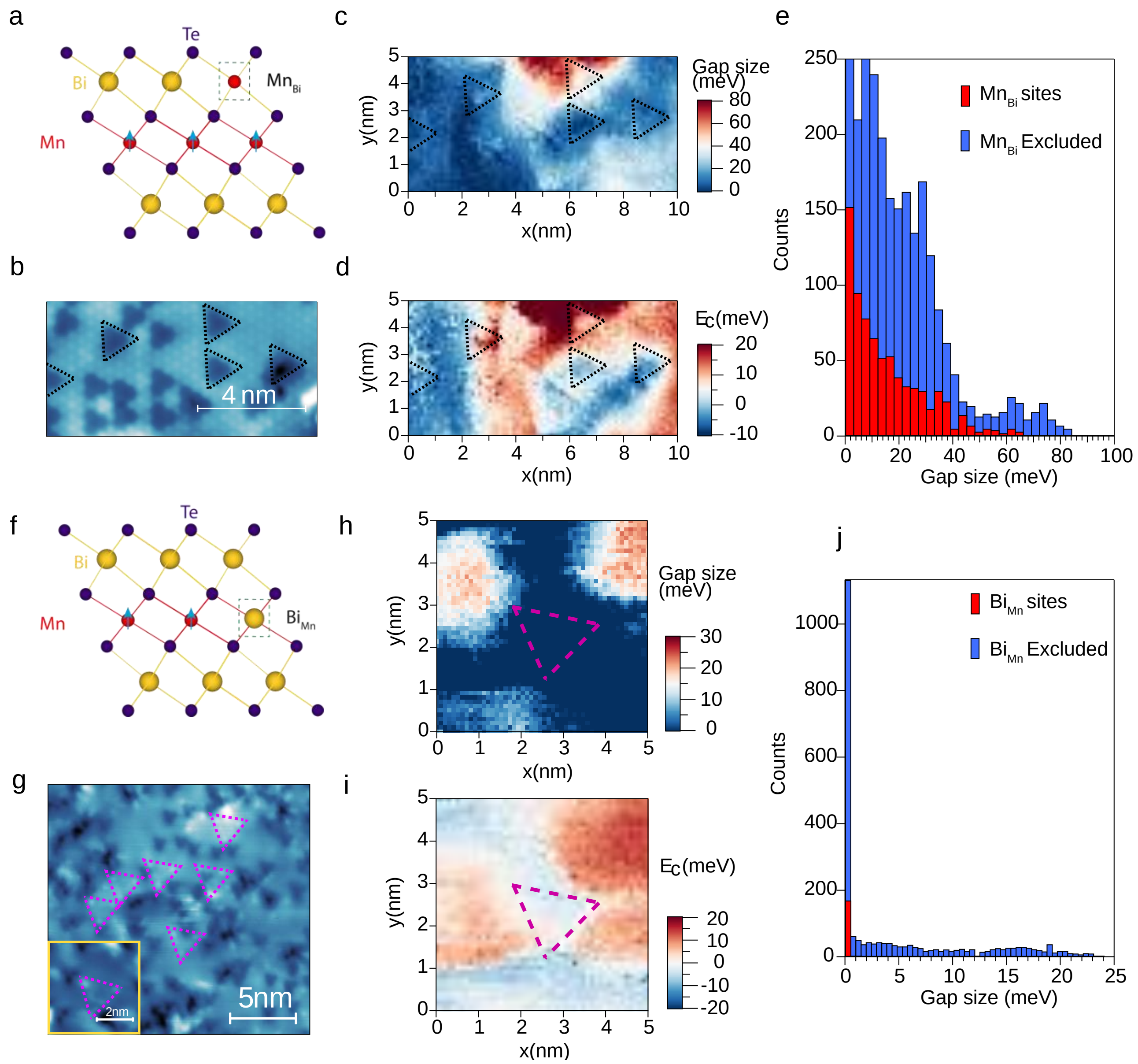

Figure 3 | Local response of the exchange gap and doping to point defects. (a) Illustration of a Mn_{Bi} defect in the lattice. **(b)** Topography of a 10×5 nm area (-150 mV, 3 nA) with Mn_{Bi} defects manifesting as dark triangles (marked in black triangles). **(c)** An exchange gap, $E_{g,ex,}$ map extracted from d*I*/d*V* spectra (-100 mV, 0.8 nA) on a 40×80 mesh for visualizing band gap fluctuation and **(d)** gap center from the same region as **(c)**. **(e)** Histograms of the $E_{g,ex}$ extracted from regions with and without Mn_{Bi} defects respectively. **(f)** Illustration of a Bi_{Mn} defect in the lattice. **(g)** Topography of a 40×40 nm area (+1.7 eV, 80 pA) with Bi_{Mn} defects which manifest as bigger bright triangles (marked as purple triangles). Insert: a 5×5 nm region where d*I*/d*V* spectra (-100 mV, 0.91 nA) on a 50×50 mesh was taken to show its effect on $E_{g,ex}$ **(h)** and doping level which is reflected on gap center **(i)**. **(j)** Histograms of $E_{g,ex}$ extracted from the defect region and region excluding the defect.

FIGURE 4

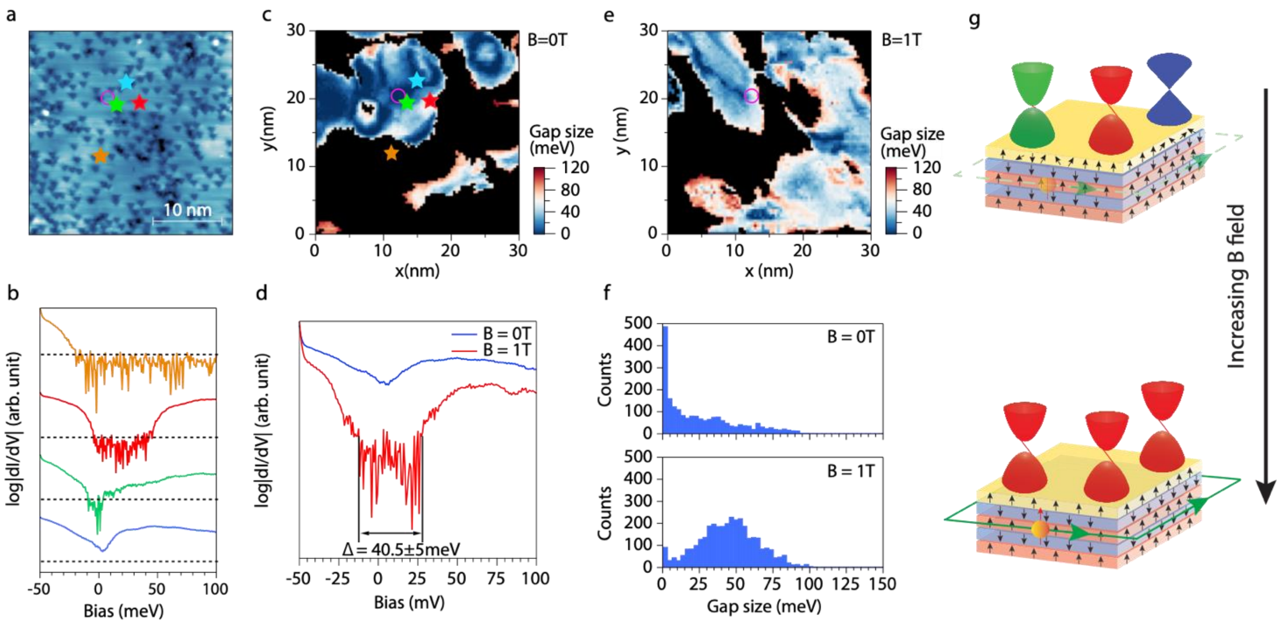

Figure 4 | Magnetic field-induced modulation of the exchange gap. (a) Topography scan (-0.5 V, 100 pA) of a 30×30 nm area where magnetic field dependent STS measurements were conducted. **(b)** Representative d*I*/d*V* spectra taken at different locations, blue: gapless regions, green: reduced-gap regions, red: large-gap regions and orange: regions where Dirac electron band is suppressed which prevents us from extracting the band gap. **(c)** Band gap map (80×80 points, -150 mV, 400 pA) of the region in **(a)** at magnetic field B = 0 T. **(d)** d*I*/d*V* spectrum taken at the position marked by purple circle in **(a)** at B = 0 T (blue) and B = 1 T (red). A magnetic Dirac gap of 40.5 meV is opened with 1 T field in a gapless region at 0 T. **(e)** Band gap map (80×80 points, -150 mV, 400 pA) of the same region in (a) at B = 1 T. Black regions in (c) and (e) correspond to the suppressed Dirac electron band regions which prevent accurate determination of the exchange gap and are excluded from the maps and subsequent histograms in **(f)**. **(f)** Histograms showing gap size at B = 0 T (upper panel) and B = 1 T (lower panel). A clear renormalization of bandgap is observed with magnetic field. **(g)** Illustration of the band gap spatial fluctuation caused by surface magnetic disorder which can be reduced significantly by applying a perpendicular magnetic field. The blue, green and red Dirac cones represent gapless, partially gapped and fully gapped regions. Their representative d*I*/d*V* curves can be found in **Figure 1(f)**. Upon applying a perpendicular magnetic field, the exchange gap in the Dirac cones increases until it reaches saturation.

References

1. Schindler F, Wang Z, Vergniory MG, Cook AM, Murani A, Sengupta S*, et al.* Higher-order topology in bismuth. *Nature Physics* 2018, **14**(9)**:** 918-924.

2. Reis F, Li G, Dudy L, Bauernfeind M, Glass S, Hanke W*, et al.* Bismuthene on a SiC substrate: A candidate for a high-temperature quantum spin Hall material. *Science* 2017, **357**(6348)**:** 287-290.

3. Tanaka Y, Ren Z, Sato T, Nakayama K, Souma S, Takahashi T*, et al.* Experimental realization of a topological crystalline insulator in SnTe. *Nature Physics* 2012, **8**(11)**:** 800-803.

4. Liu C, Wang Y, Li H, Wu Y, Li Y, Li J*, et al.* Robust axion insulator and Chern insulator phases in a two-dimensional antiferromagnetic topological insulator. *Nature Materials* 2020, **19**(5)**:** 522-527.

5. Hasan MZ, Kane CL. Colloquium: Topological insulators. *Reviews of Modern Physics* 2010, **82**(4)**:** 3045-3067.

6. Bestwick AJ, Fox EJ, Kou X, Pan L, Wang KL, Goldhaber-Gordon D. Precise Quantization of the Anomalous Hall Effect near Zero Magnetic Field. *Physical Review Letters* 2015, **114**(18)**:** 187201.

7. Chang C-Z, Zhao W, Kim DY, Zhang H, Assaf BA, Heiman D*, et al.* High-precision realization of robust quantum anomalous Hall state in a hard ferromagnetic topological insulator. *Nature Materials* 2015, **14**(5)**:** 473-477.

8. Lian B, Sun X-Q, Vaezi A, Qi X-L, Zhang S-C. Topological quantum computation based on chiral Majorana fermions. *Proceedings of the National Academy of Sciences* 2018, **115**(43)**:** 10938-10942.

9. Qi X-L, Hughes TL, Zhang S-C. Chiral topological superconductor from the quantum Hall state. *Physical Review B* 2010, **82**(18)**:** 184516.

10. Huckestein B. Scaling theory of the integer quantum Hall effect. *Reviews of Modern Physics* 1995, **67**(2)**:** 357-396.

11. Sondhi SL, Girvin SM, Carini JP, Shahar D. Continuous quantum phase transitions. *Reviews of Modern Physics* 1997, **69**(1)**:** 315-333.

12. Moreau N, Brun B, Somanchi S, Watanabe K, Taniguchi T, Stampfer C*, et al.* Upstream modes and antidots poison graphene quantum Hall effect. *Nature Communications* 2021, **12**(1)**:** 4265.

13. Marguerite A, Birkbeck J, Aharon-Steinberg A, Halbertal D, Bagani K, Marcus I*, et al.* Imaging work and dissipation in the quantum Hall state in graphene. *Nature* 2019, **575**(7784)**:** 628-633.

14. Maciejko J, Liu C, Oreg Y, Qi X-L, Wu C, Zhang S-C. Kondo Effect in the Helical Edge Liquid of the Quantum Spin Hall State. *Physical Review Letters* 2009, **102**(25)**:** 256803.

15. Liu C, Culcer D, Wang Z, Edmonds MT, Fuhrer MS. Helical Edge Transport in Millimeter-Scale Thin Films of Na3Bi. *Nano Letters* 2020, **20**(9)**:** 6306-6312.

16. Kane CL, Mele EJ. Quantum Spin Hall Effect in Graphene. *Physical Review Letters* 2005, **95**(22)**:** 226801.

17. Fu L, Kane CL, Mele EJ. Topological Insulators in Three Dimensions. *Physical Review Letters* 2007, **98**(10)**:** 106803.

18. Liu M, Wang W, Richardella AR, Kandala A, Li J, Yazdani A*, et al.* Large discrete jumps observed in the transition between Chern states in a ferromagnetic topological insulator. *Science Advances* 2016, **2**(7)**:** e1600167.

19. Lee I, Kim CK, Lee J, Billinge SJL, Zhong R, Schneeloch JA*, et al.* Imaging Dirac-mass disorder from magnetic dopant atoms in the ferromagnetic topological insulator Crx(Bi0.1Sb0.9)2-xTe3. *Proceedings of the National Academy of Sciences* 2015, **112**(5)**:** 1316-1321.

20. Otrokov MM, Klimovskikh II, Bentmann H, Estyunin D, Zeugner A, Aliev ZS*, et al.* Prediction and observation of an antiferromagnetic topological insulator. *Nature* 2019, **576**(7787)**:** 416-422.

21. Li J, Li Y, Du S, Wang Z, Gu B-L, Zhang S-C*, et al.* Intrinsic magnetic topological insulators in van der Waals layered MnBi2Te4-family materials. *Science Advances* 2019, **5**(6)**:** eaaw5685.

22. Otrokov MM, Rusinov IP, Blanco-Rey M, Hoffmann M, Vyazovskaya AY, Eremeev SV*, et al.* Unique Thickness-Dependent Properties of the van der Waals Interlayer Antiferromagnet MnBi2Te4 Films. *Physical Review Letters* 2019, **122**(10)**:** 107202.

23. Deng Y, Yu Y, Shi MZ, Guo Z, Xu Z, Wang J*, et al.* Quantum anomalous Hall effect in intrinsic magnetic topological insulator MnBi2Te4. *Science* 2020, **367**(6480)**:** 895-900.

24. Bai Y, Li Y, Luan J, Liu R, Song W, Chen Y*, et al.* Quantized anomalous Hall resistivity achieved in molecular beam epitaxy-grown MnBi2Te4 thin films. *arXiv preprint arXiv:220603773* 2022.

25. Garrity KF, Chowdhury S, Tavazza FM. Topological surface states of MnBi2Te4 at finite temperatures and at domain walls. *Physical Review Materials* 2021, **5**(2)**:** 024207.

26. Yuan Y, Wang X, Li H, Li J, Ji Y, Hao Z*, et al.* Electronic States and Magnetic Response of MnBi2Te4 by Scanning Tunneling Microscopy and Spectroscopy. *Nano Letters* 2020, **20**(5)**:** 3271-3277.

27. Huang Z, Du M-H, Yan J, Wu W. Native defects in antiferromagnetic topological insulator MnBi2Te4. *Physical Review Materials* 2020, **4**(12)**:** 121202.

28. Garnica M, Otrokov MM, Aguilar PC, Klimovskikh II, Estyunin D, Aliev ZS*, et al.* Native point defects and their implications for the Dirac point gap at MnBi2Te4(0001). *npj Quantum Materials* 2022, **7**(1)**:** 7.

29. Liu M, Lei C, Kim H, Li Y, Frammolino L, Yan J*, et al.* Visualizing the interplay of Dirac mass gap and magnetism at nanoscale in intrinsic magnetic topological insulators. *Proceedings of the National Academy of Sciences* 2022, **119**(42)**:** e2207681119.

30. Hor YS, Roushan P, Beidenkopf H, Seo J, Qu D, Checkelsky JG*, et al.* Development of ferromagnetism in the doped topological insulator Bi2-xMnxTe3. *Physical Review B* 2010, **81**(19)**:** 195203.

31. Beidenkopf H, Roushan P, Seo J, Gorman L, Drozdov I, Hor YS*, et al.* Spatial fluctuations of helical Dirac fermions on the surface of topological insulators. *Nature Physics* 2011, **7**(12)**:** 939-943.

32. Trang CX, Li Q, Yin Y, Hwang J, Akhgar G, Di Bernardo I*, et al.* Crossover from 2D Ferromagnetic Insulator to Wide Band Gap Quantum Anomalous Hall Insulator in Ultrathin MnBi2Te4. *ACS Nano* 2021, **15**(8)**:** 13444-13452.

33. Rienks EDL, Wimmer S, Sánchez-Barriga J, Caha O, Mandal PS, Růžička J*, et al.* Large magnetic gap at the Dirac point in Bi2Te3/MnBi2Te4 heterostructures. *Nature* 2019, **576**(7787)**:** 423-428.

34. Lüpke F, Pham AD, Zhao Y-F, Zhou L-J, Lu W, Briggs E*, et al.* Local manifestations of thickness-dependent topology and edge states in the topological magnet MnBi2Te4. *Physical Review B* 2022, **105**(3)**:** 035423.

35. Xu H-K, Gu M, Fei F, Gu Y-S, Liu D, Yu Q-Y*, et al.* Observation of Magnetism-Induced Topological Edge State in Antiferromagnetic Topological Insulator MnBi4Te7. *ACS Nano* 2022, **16**(6)**:** 9810-9818.

36. Jia J, Marcellina E, Das A, Lodge MS, Wang B, Ho D-Q*, et al.* Tuning the many-body interactions in a helical Luttinger liquid. *Nature Communications* 2022, **13**(1)**:** 6046.

37. Alpichshev Z, Analytis JG, Chu JH, Fisher IR, Chen YL, Shen ZX*, et al.* STM Imaging of Electronic Waves on the Surface of Bi2Te3: Topologically Protected Surface States and Hexagonal Warping Effects. *Physical Review Letters* 2010, **104**(1)**:** 016401.

38. Collins JL, Tadich A, Wu W, Gomes LC, Rodrigues JNB, Liu C*, et al.* Electric-field-tuned topological phase transition in ultrathin Na3Bi. *Nature* 2018, **564**(7736)**:** 390-394.

39. Padmanabhan H, Stoica VA, Kim PK, Poore M, Yang T, Shen X*, et al.* Large Exchange Coupling Between Localized Spins and Topological Bands in MnBi2Te4. *Advanced Materials* 2022, **34**(49)**:** 2202841.

40. Li B, Yan JQ, Pajerowski DM, Gordon E, Nedić AM, Sizyuk Y*, et al.* Competing Magnetic Interactions in the Antiferromagnetic Topological Insulator MnBi2Te4. *Physical Review Letters* 2020, **124**(16)**:** 167204.

41. Sass PM, Kim J, Vanderbilt D, Yan J, Wu W. Robust A-Type Order and Spin-Flop Transition on the Surface of the Antiferromagnetic Topological Insulator MnBi2Te4. *Physical Review Letters* 2020, **125**(3)**:** 037201.

42. Shikin A, Makarova T, Eryzhenkov A, Usachov DY, Estyunin D, Glazkova D*, et al.* Factors influencing the energy gap in topological states of antiferromagnetic MnBi2Te4. *arXiv preprint arXiv:220507501* 2022.

43. Bac SK, Koller K, Lux F, Wang J, Riney L, Borisiak K*, et al.* Topological response of the anomalous Hall effect in MnBi2Te4 due to magnetic canting. *npj Quantum Materials* 2022, **7**(1)**:** 46.

44. Yang S, Xu X, Zhu Y, Niu R, Xu C, Peng Y*, et al.* Odd-Even Layer-Number Effect and Layer-Dependent Magnetic Phase Diagrams in MnBi2Te4. *Physical Review X* 2021, **11**(1)**:** 011003.

45. He K, Xue Q-K. The Road to High-Temperature Quantum Anomalous Hall Effect in Magnetic Topological Insulators. *SPIN* 2019, **09:** 1940016.

46. Fu H, Liu C-X, Yan B. Exchange bias and quantum anomalous Hall effect in the MnBi2Te4/CrI3 heterostructure. *Science Advances* 2020, **6**(10)**:** eaaz0948.

47. Otrokov MM, Menshchikova TV, Vergniory MG, Rusinov IP, Yu Vyazovskaya A, Koroteev YM*, et al.* Highly-ordered wide bandgap materials for quantized anomalous Hall and magnetoelectric effects. *2D Materials* 2017, **4**(2)**:** 025082.

48. Li Q, Trang CX, Wu W, Hwang J, Cortie D, Medhekar N*, et al.* Large Magnetic Gap in a Designer Ferromagnet–Topological Insulator–Ferromagnet Heterostructure. *Advanced Materials* 2022, **34**(21)**:** 2107520.

49. Bhattacharyya S, Akhgar G, Gebert M, Karel J, Edmonds MT, Fuhrer MS. Recent Progress in Proximity Coupling of Magnetism to Topological Insulators. *Advanced Materials* 2021, **33**(33)**:** 2007795.

50. Zhu T, Bishop AJ, Zhou T, Zhu M, O'Hara DJ, Baker AA*, et al.* Synthesis, Magnetic Properties, and Electronic Structure of Magnetic Topological Insulator MnBi2Se4. *Nano Letters* 2021, **21**(12)**:** 5083-5090.

Supporting Information

Imaging the breakdown and restoration of topological protection in magnetic topological insulator $MnBi_2Te_4$

Qile Li[1,2*], Iolanda Di Bernardo[1,2], Johnathon Maniatis[1], Daniel McEwen[1,2], Amelia D. Celorrio[1,2], Mohammad T. H. Bhuiyan[1], Mengting Zhao[1,2,3], Anton Tadich[3], Liam Watson[1,2], Benjamin Lowe[1,2], Thi-Hai-Yen Vu[1], Chi Xuan Trang[1,2], Jinwoong Hwang[4,5], Sung-Kwan Mo[4], Michael S. Fuhrer[1,2], Mark T. Edmonds[1,2,6*]

[1]School of Physics and Astronomy, Monash University, Clayton, VIC, Australia

[2]ARC Centre for Future Low Energy Electronics Technologies, Monash University, Clayton, VIC, Australia

[3]Australian Synchrotron

[4]Advanced Light Source, Lawrence Berkeley National Laboratory, Berkeley, CA, 94720 USA

[5]Department of Physics and Institute of Quantum Convergence Technology, Kangwon National University, Chuncheon, 24341, Republic of Korea

[6]ANFF-VIC Technology Fellow, Melbourne Centre for Nanofabrication, Victorian Node of the Australian National Fabrication Facility, Clayton, VIC 3168, Australia

*Corresponding Author mark.edmonds@monash.edu and qile.li@monash.edu

Table of Contents

1. Structure and surface characterization of 5 SL $MnBi_2Te_4$ epitaxial film

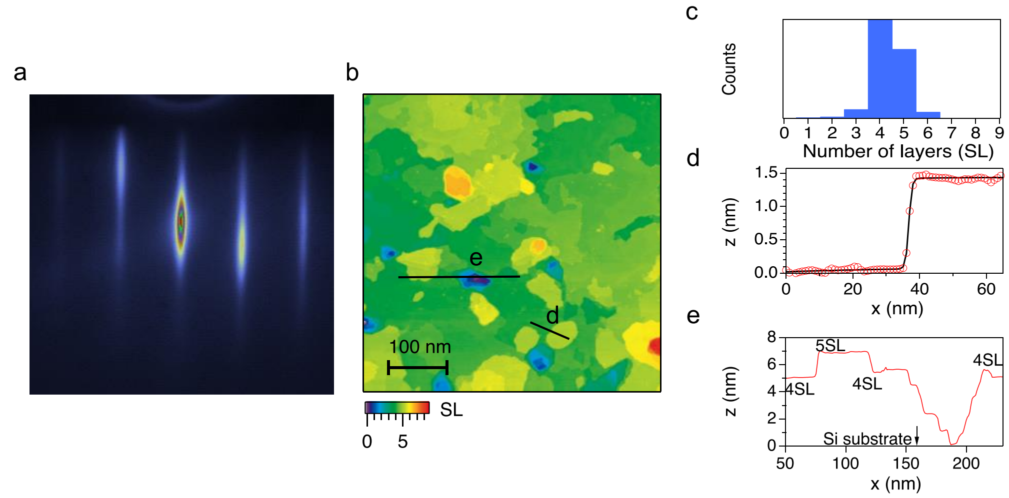

Figure S1 | Structure and surface characterization of ultra-thin $MnBi_2Te_4$ epitaxial film. (a) Reflection high energy electron diffraction of the thin film showing strong sharp streaks which indicates high crystallinity. **(b)** STM topography scan on a 500×500 nm area (-2 V, 20 pA). **(c)** Histogram of number of SLs from **(b)** which shows majority of 4 SL terrace (green) with regions of 5 SL terrace (yellow). The thickness is determined from the depth of pinholes (dark blue and purple regions) which represent the Si substrate. **(d)** A line profile extracted from one of the 4 SL-5 SL step edges as marked by the black line in **(b)** and fitting to an edge function, which yields a step edge of 1.39 nm. **(e)** A line profile extracted across a pin hole to show the thickness of terraces as marked by the black line in **(b)**.

2. Doping shift due to different Si(111) substrates.

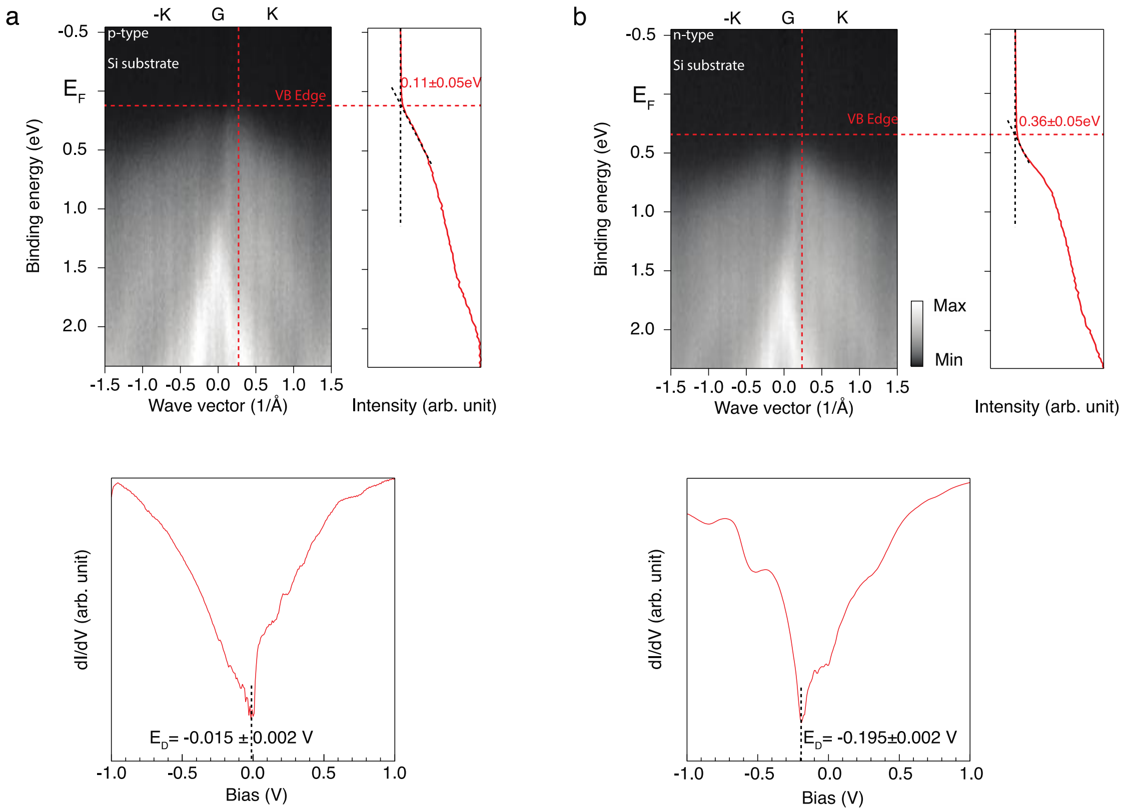

Figure S2 | ARPES spectra and representative scanning tunnelling spectroscopy (STS) spectra of 5SL $MnBi_2Te_4$ grown on (a) p-type and (b) n-type silicon substrates respectively using He-II light source (hv = 21.2eV). The Dirac cone is not visible in the ARPES spectra because of the low photon flux of the helium lamp. The energy distribution curve is taken at the wave vector marked by the red dashed lines and are plotted on the right of each spectrum. The edge of valence bands is determined from ARPES and the Dirac point energy is determined from the minima in the STS spectra, which are used for estimating the doping level of the samples. A doping level difference between the two types of Si (111) substrates is ~180 meV.

3. Schematics and determination of Bi_{Mn} defects

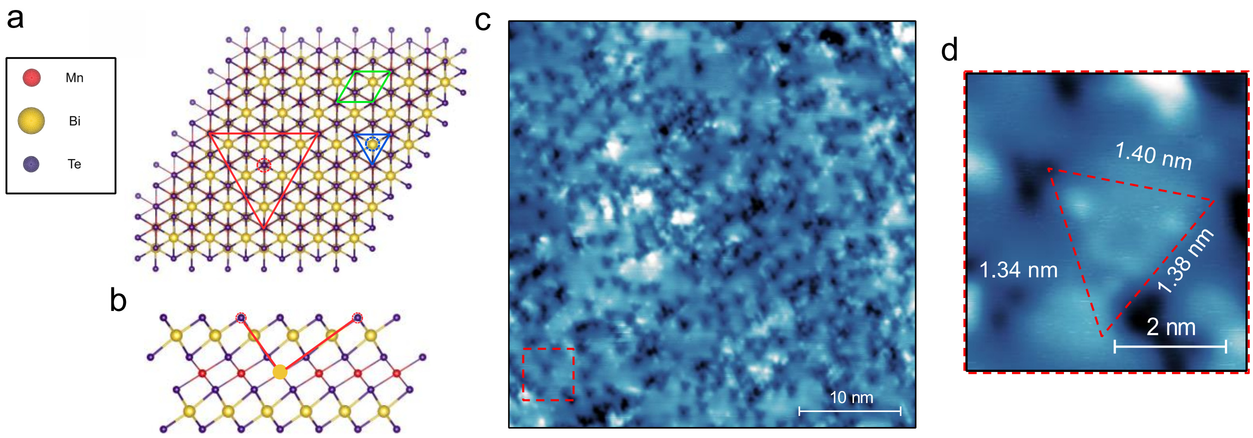

Figure S3 | Schematics and determination of Bi_{Mn} defects. (a) Top view of the crystal structure with primitive cell (green), Mn_{Bi} defect (blue) and Bi_{Mn} defect (red) marked. **(b)** Side view of the Bi_{Mn} defect in a SL. The Te atoms on the very top appear as bright triangles at positive bias because of DOS propagated along Te p_z orbitals centered around Bi_{Mn} defect. The three Te atoms appear to be more positively charged due to the extra charge from a Bi^{3+} ion replacing Mn^{2+} ion. **(c)** Topography scan on a 40×40 nm area (+1.7 V, 80 pA) showing Bi_{Mn} defects on an atomically flat terrace. **(d)** A zoom-in image of the selected region marked by red box in **(c)** for extracting dimensions of defects. The length of the triangle's edge is around 1.35 nm which is close to the theoretical value of 1.31 nm. The same orientation of Mn_{Bi} dark triangles and Bi_{Mn} bright triangles also matches the schematics **(a)**.

4. Determination of Dirac band gap and gap center from dI/dV spectrum

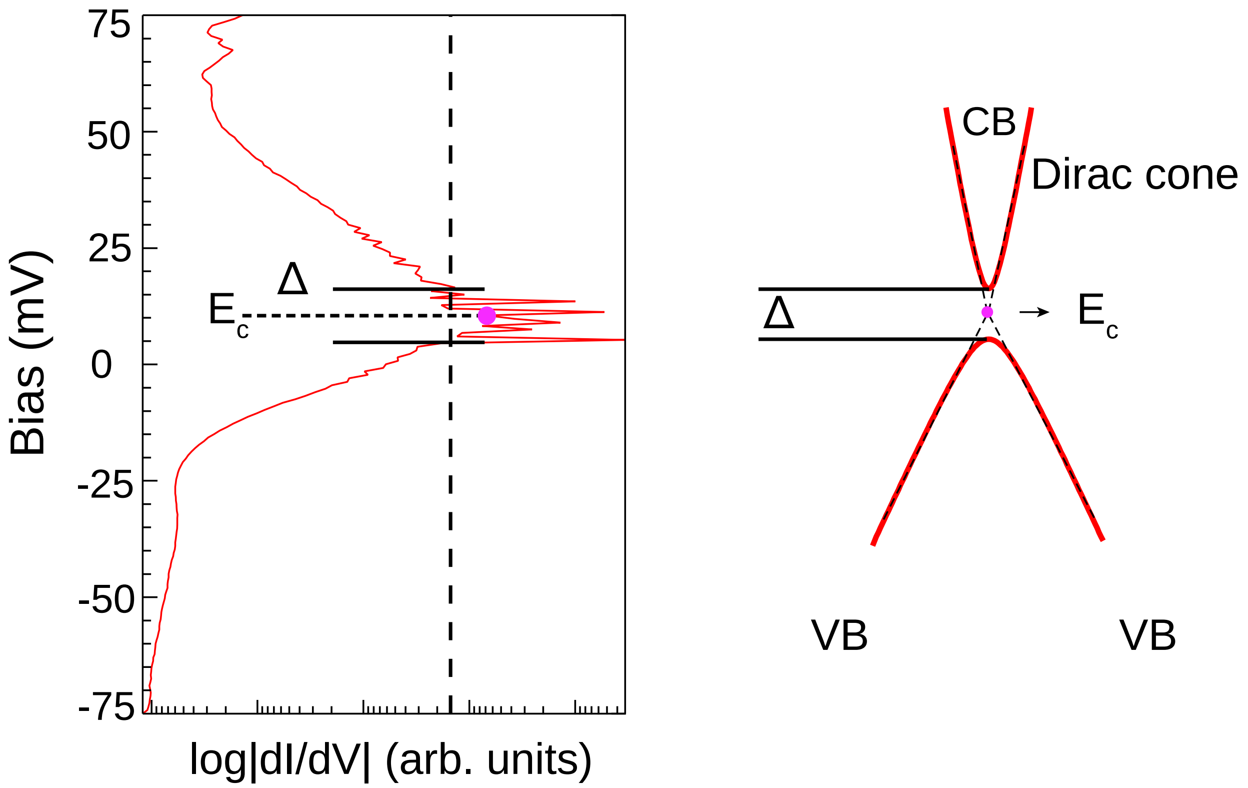

Figure S4| Determination of Dirac band gap and gap center from *dI/dV* spectrum. Left, a dI/dV spectrum taken on a 5 SL $MnBi_2Te_4$ terrace showing a gap in the Dirac states. **Right,** a schematic of the Dirac cone corresponding to the dI/dV spectrum on the left. The Dirac cone in 5 SL $MnBi_2Te_4$ is lifted out of VB and resides between bulk conduction band (CB) and bulk valence band (VB). The Dirac gap is extracted based on the noise floor of the dI/dV spectrum (black dashed line). The width of the region between valence and conduction band edges corresponds to the size of Dirac gap Δ as illustrated on the right figure.

To extract the Dirac gap from STS spectra, the edges of valence band and conduction band are determined from the spectrum as the onset of dI/dV intensity above the noise floor (black dashed line in **Figure S4** left). A logarithmic scale is chosen for dI/dV intensity axis to better account for the sudden change of intensity near the band edge. The local doping level can be estimated from the center of Dirac gap which can be calculated using

$$E_c = \frac{\int f(\boldsymbol{r}, E) E dE}{\int f(\boldsymbol{r}, E) dE}$$

where $f(\boldsymbol{r}, E)$=1 if STS curve $g(\boldsymbol{r}, E)$ < noise floor and $f(\boldsymbol{r}, E)$=0 otherwise[19]. This is essentially averaging the position of center of gap and is equivalent to extrapolating the gapped Dirac bands as shown in **Figure S4** right. Since the Dirac cone is now gapped by magnetic order and Dirac point no longer exists, the gap center (purple dot) is a good measure of the local doping shift by defects.

5. Bias dependent and set point current dependent STS measurements

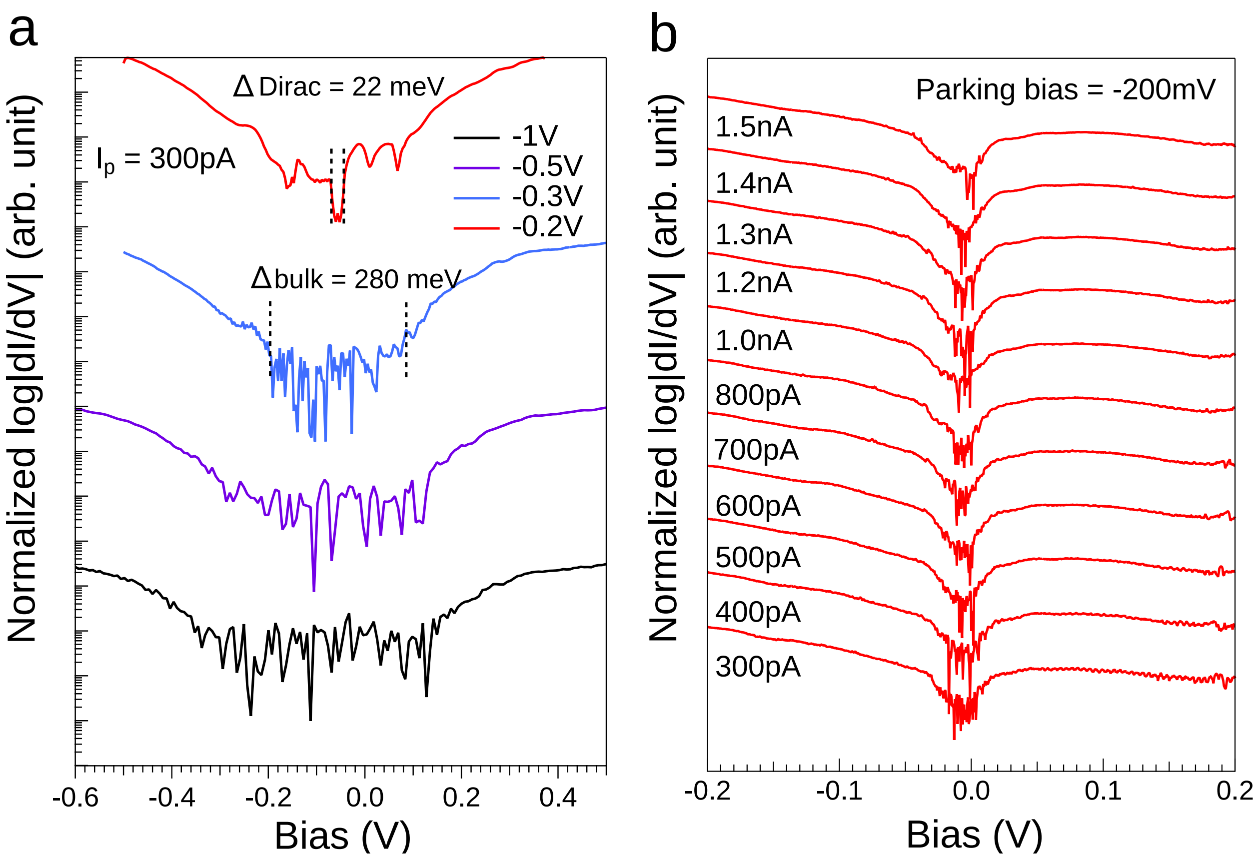

Figure S5 | Bias dependent and set point current dependent STS measurements. (a) STS spectra taken at different bias, the tip-sample tunneling junction decreases as the bias voltage decreases bias, resulting in a stronger signal which is necessary to observe the Dirac bands in dI/dV. **(b)** STS spectra taken at various set point current and fixed parking bias of -200 mV showing a Dirac gap. The band edge position shows minimal shift at different set point current and bias, indicating minimal tip induced band bending.

As shown in **Figure S5(a)**, the STS spectrum on the terrace only shows a large bulk gap at parking bias of -1 V. As the tip is parked closer to the surface by decreasing bias, more features in the spectrum, including surface states and Dirac band gap, can be resolved within the bulk gap. Therefore, we choose parking bias of typical value -0.2 V and 300 pA for our STS maps. In **Figure S5(b)**, STS spectra taken on the same location and fixed bias but with varying set point current are plotted and offset manually. From set point current of 300 pA to 1.5 nA, there is no significant shift of band edges or increase of band gap. In the case of tip induced band bending, increasing the set point current will increase the band bending and lead to increase of band gap. Apparently, the most noticeable change in the **Figure S5(b)** is reduced noise in the spectra while the overall shape and position of the band edge stay the unchanged. Therefore, we can rule out contribution from tip induced band bending to the band gap.

6. Topography image and dI/dV map of the 5SL to 4SL edge in Figure 2 at other bias values.

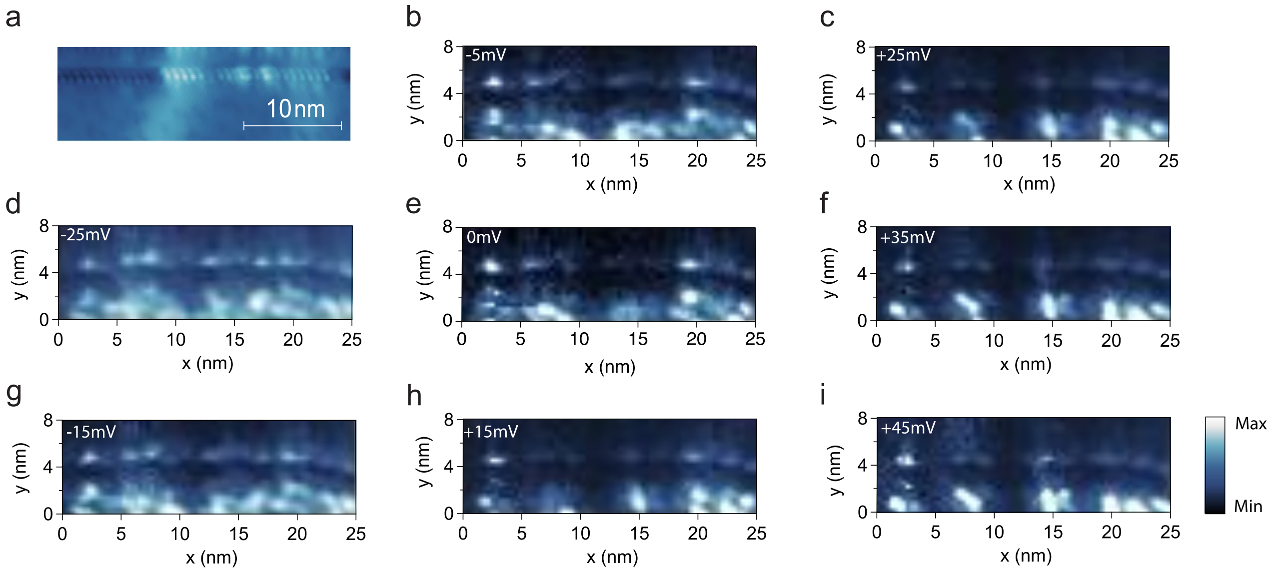

Figure S6| (a) Topography image (-1 V, 30 pA) and (b)-(i) d*I*/d*V* maps (-0.15 V, 400 pA) of the edge in Figure 2 at other bias values.

7. Topography image and dI/dV map of a 4SL to 3SL edge.

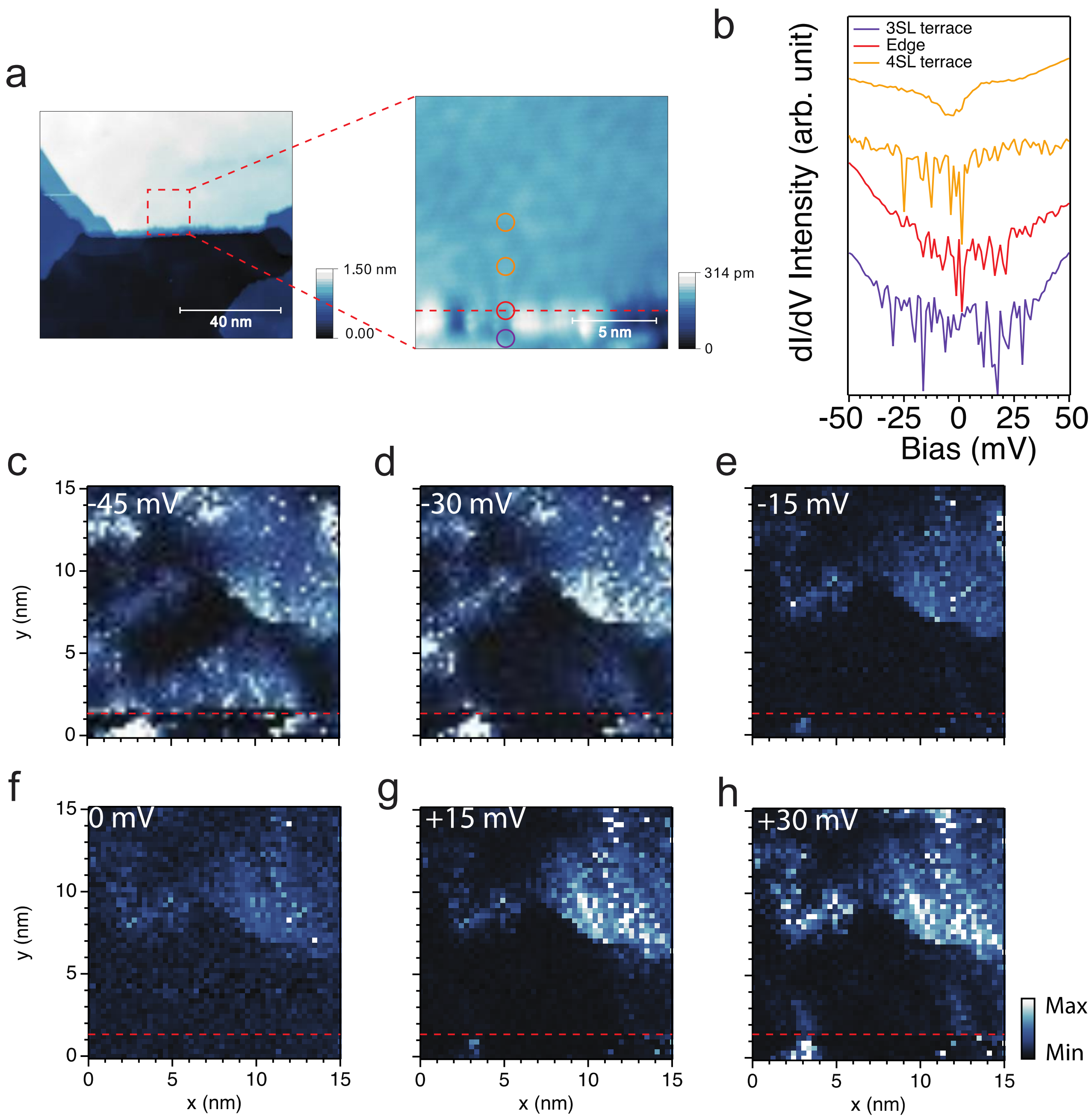

Figure S7 | d*I*/d*V* maps on an even-to-odd edge at several bias across the band gap. (a) topography scans (-2.5 V, 20 pA) of the edge, atomic-resolution scan (-2.5V, 20 pA) where maps are taken and (b) STS spectra (-0.15V, 400 pA) at locations marked. The terrace edge is marked by the red dash line. (c) to (h) d*I*/d*V* maps (-0.15V, 400 pA) at various bias with location of edge marked.

8. Visualizing the gapless edge state and its coupling to bulk metallic states.

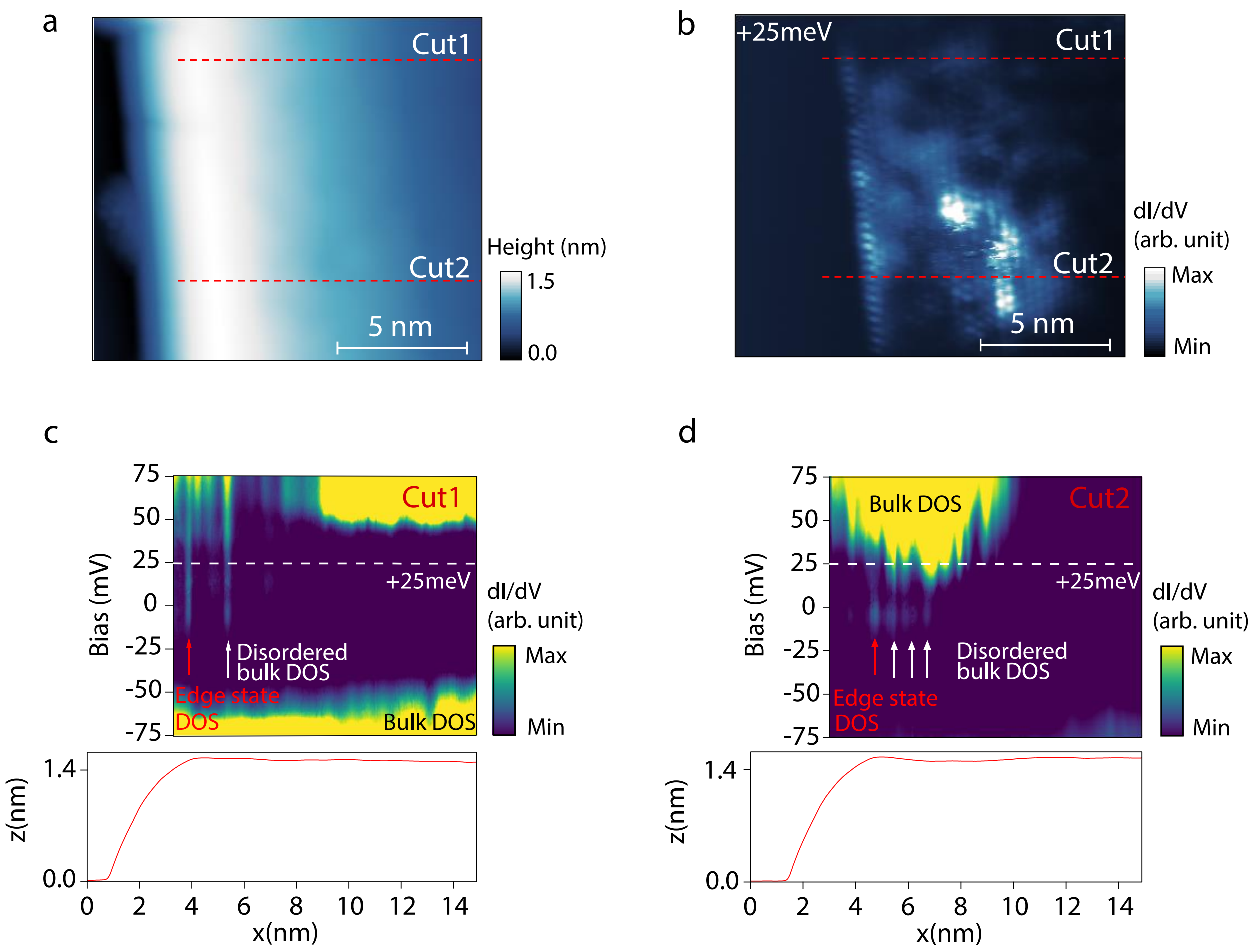

Figure S8 | Visualizing the gapless edge state and its coupling to bulk metallic states. (a) Topography image (-1 V, 50 pA) taken across a step edge from 4 SL to 5 SL $MnBi_2Te_4$. **(b)** d*I*/d*V* map at +25 mV bias (40 pA) in the same region as (a) to show the spatial distribution of the edge state. **(c),(d)** d*I*/d*V* spectra (-0.15V, 350pA) and height profile taken across the edge from top of the area and bottom of the area respectively marked by red dashed lines. The horizontal axis of the spectra is aligned with the height profile. The edge state is marked by red arrow and other peaks are attributed to disordered bulk states which is marked by white arrows. The white horizontal dashed line shows the bias at which **(b)** is taken.

9. Representative dI/dV spectra from STS map around Mn_{Bi} defects

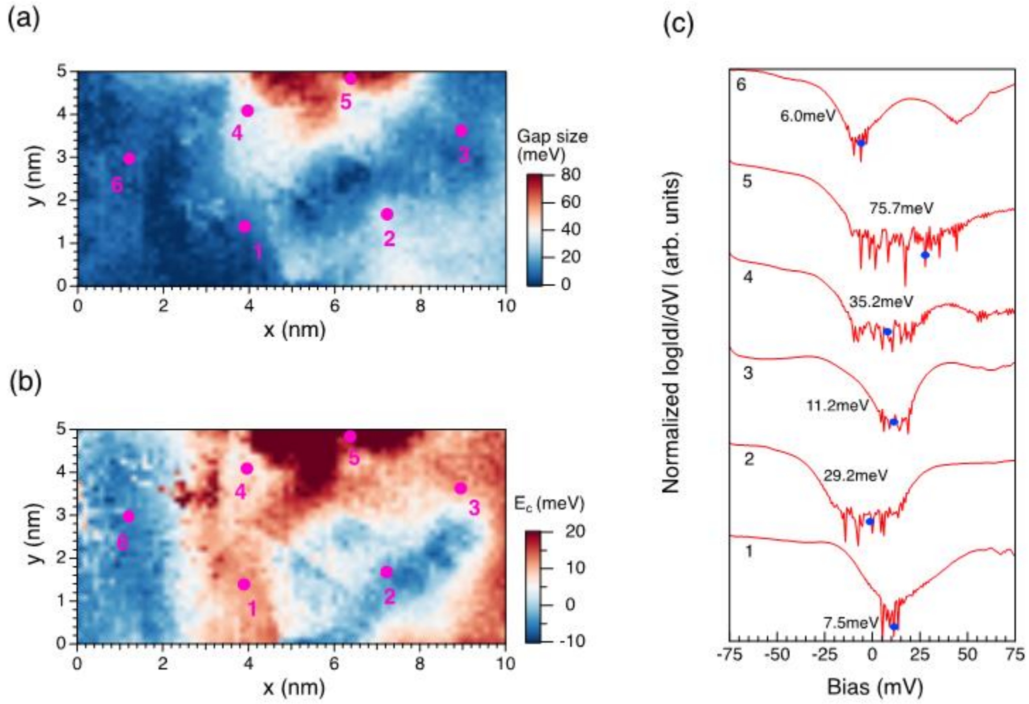

Figure S9 | Representative d*I*/d*V* spectra from STS map around Mn_{Bi} defects. **(a)** Band gap map extracted from d*I*/d*V* spectra (-0.1 V, 800 pA) with some locations where STS shown marked in green. **(b)** Gap center map extracted from d*I*/d*V* spectra. **(c)** Stack plot of d*I*/d*V* spectra taken from locations in **(a)-(b)**, where band gap values are marked on each d*I*/d*V* spectrum, and gap center positions calculated using method discussed in **Figure S4** are marked by blue points.

10. Topography scan of the area in Figure 4 to show the alignment of the scan region.

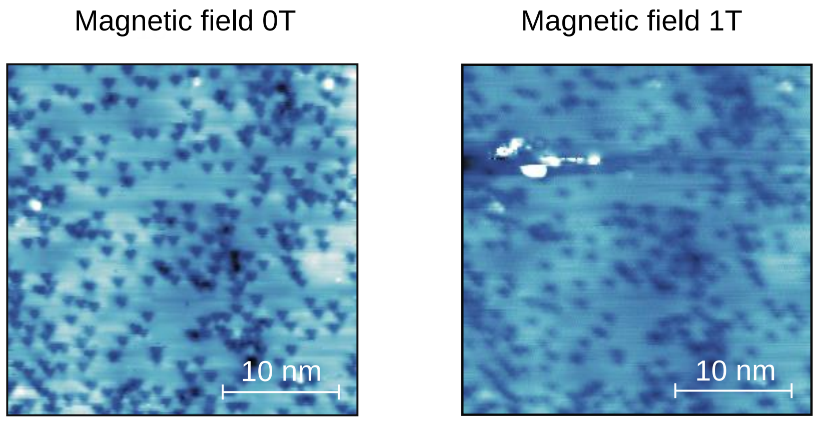

Figure S10 | Topography scans (both taken at -0.5 V, 100 pA) of the region for band gap mapping in Figure 4 at 0T and 1T.

11. Figure 4 statistical analysis of regions with unsuppressed CB at both 0T and 1T

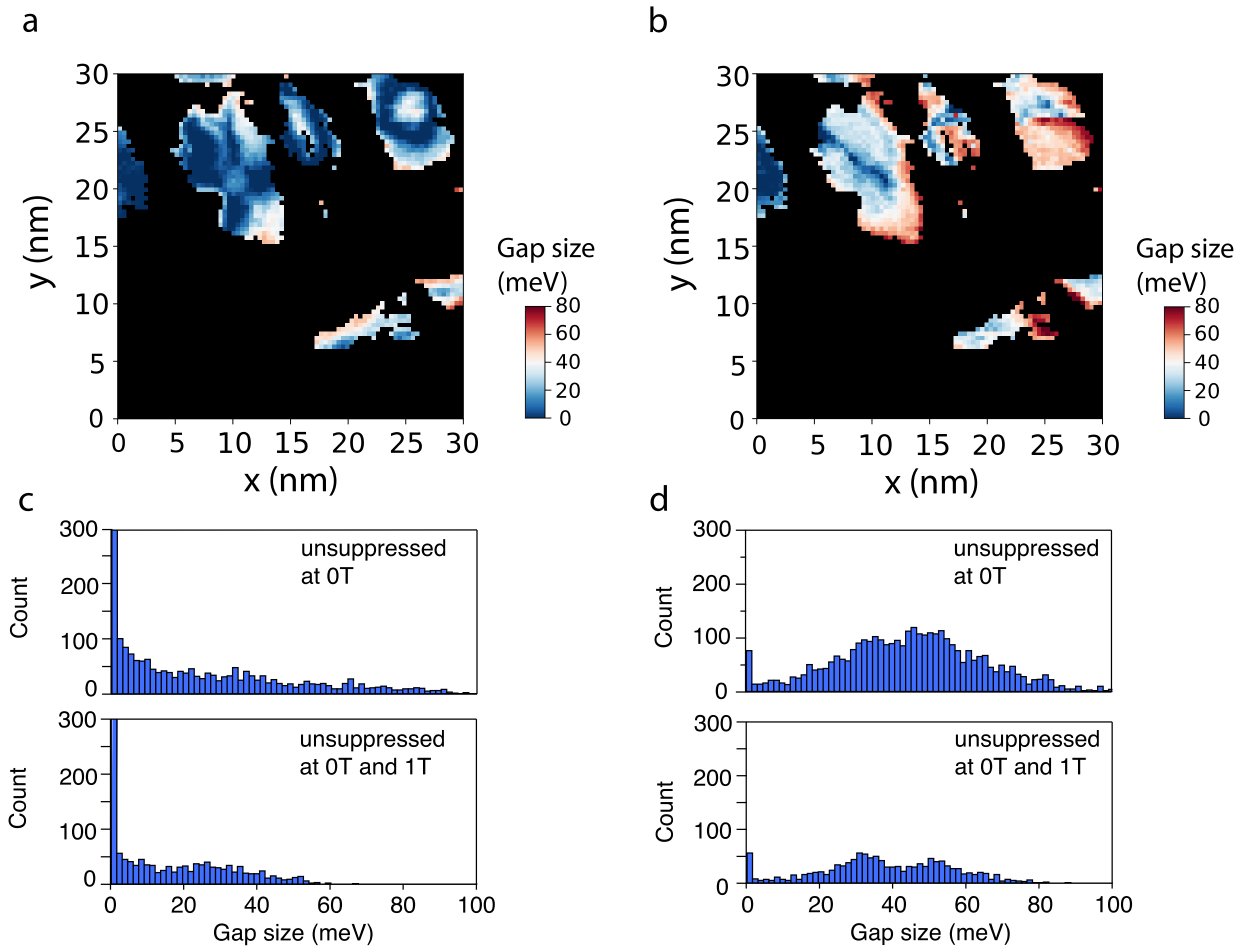

e

Average	17.2 meV
Standard deviation	16.0 meV
Skewness	0.62

f

Average	37.8 meV
Standard deviation	18.1 meV
Skewness	-0.09

Figure S11 | Statistical analysis of regions with unsuppressed CB at both 0T and 1T. (a)-(b), $E_{g,ex}$ map. **(c)-(d)**, their corresponding histogram, and **(e)-(f)**, statistical information extracted from the histograms.

In **Figure S11**, the histograms are taken from regions where the conduction band intensity is not suppressed at 0T or 1T. The analysis shows similar results as in **Figure 4**, with an increase in the average band gap size of 20.6meV. Interestingly the histogram in **Fig. S11(d)** appears to be more bimodal where the lower gap size mode corresponds to the weight shift from gapless to medium size gap and upper mode corresponds to shift from regions with medium size gap to fully gapped ones in a 1T magnetic field. Overall, regardless of the analysis method, this region shows significant increase of Dirac gap and reduction of skewness relative to a normal distribution in a 1T magnetic field.

12.Magnetic field dependent Dirac gap map

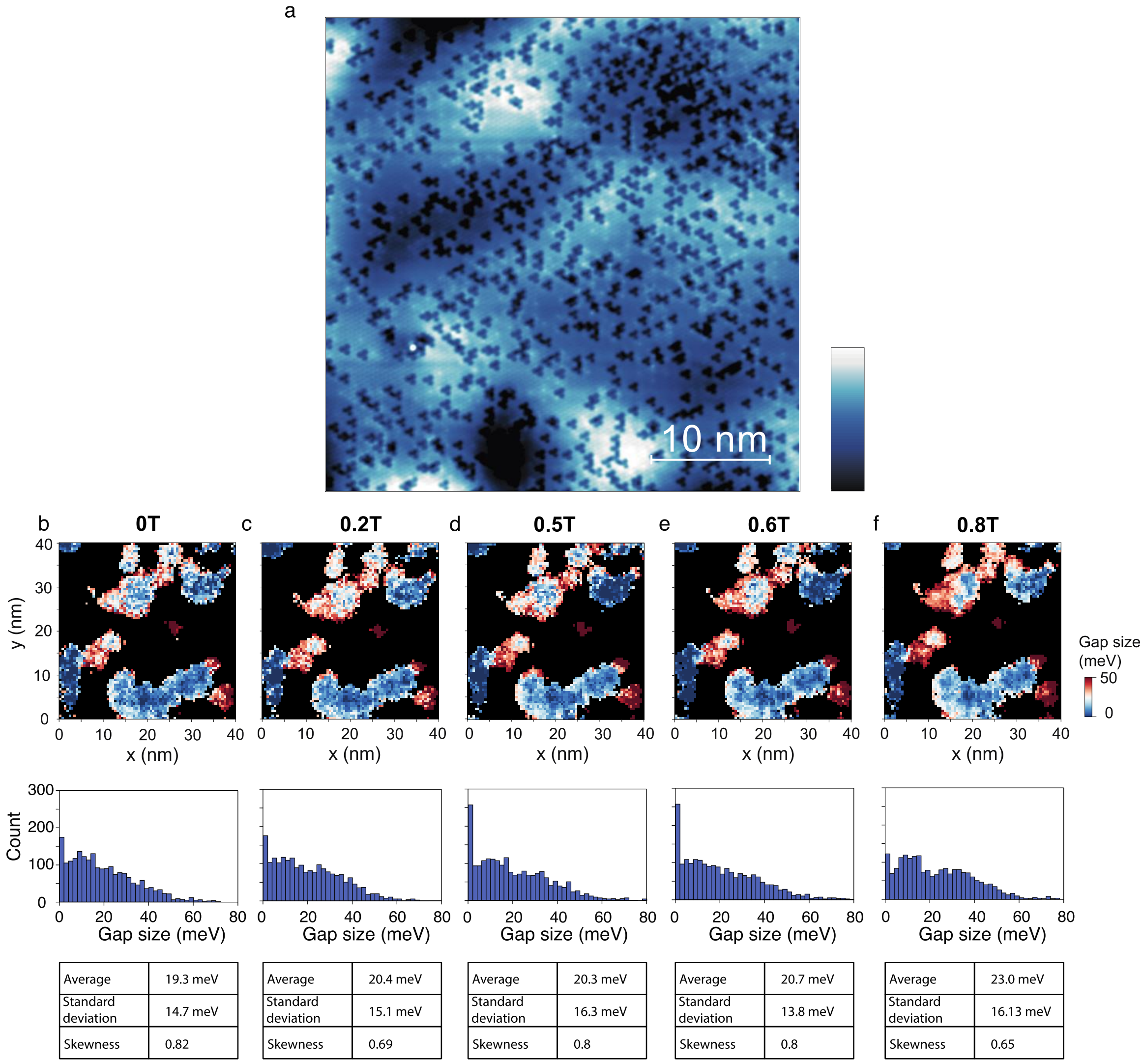

Figure S12 | Magnetic field dependent Dirac gap map and their corresponding histogram and statistical information. (a) Topography scan of the map area (40× 40 nm, -1 V, 100 pA). (b) – (f) Magnetic field dependent band gap maps (-0.15 V, 400 pA, 75×75 pixels), their histograms and statistic information.

The evolution of the histogram is very small below 0.6T and there is a sudden increase of count of gapless state. We assign this anomaly to the realigning process of Mn^{2+} moments that are initially oriented opposite to magnetic field due to magnetic disorder. The reduction of the effective out-of-plane magnetization in some regions results in the temporary increase of gapless state. At 0.8T, the count of gapless states is greatly reduced, and the bimodal feature emerges in the histogram, which is similar to the bimodal behavior in **Fig.S11(d)**.

13. Dirac band gap maps from region with large number of Bi_{Mn} defects

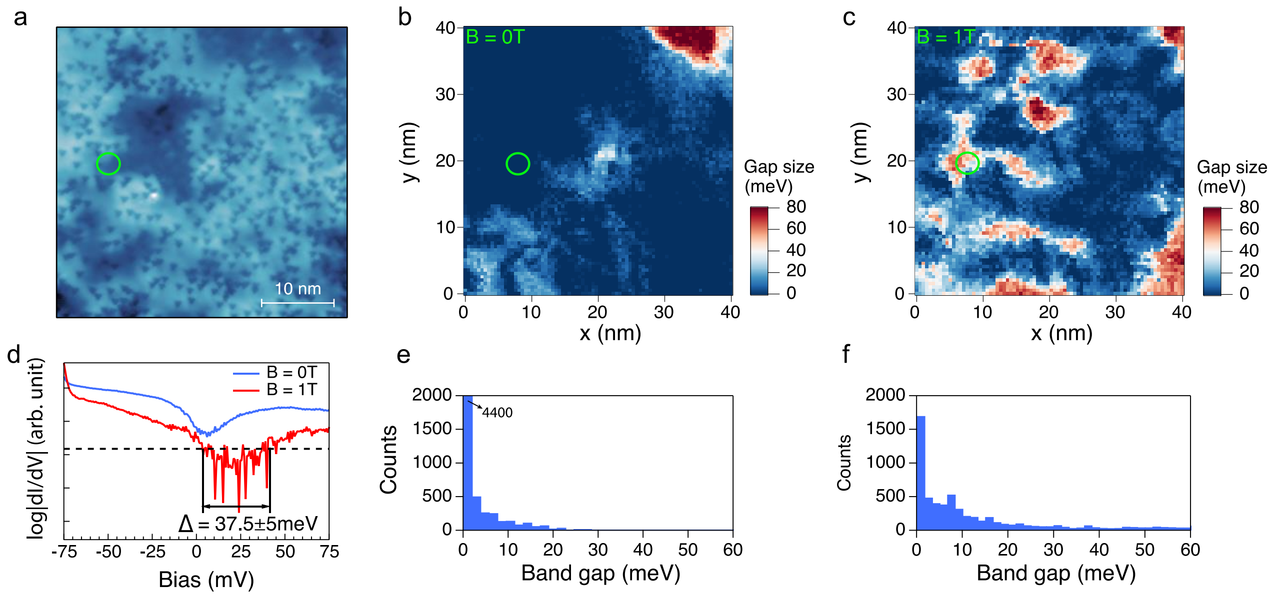

Figure S13 | Dirac band gap maps with/without magnetic field showing band gap fluctuation from region with Bi_{Mn} defects. (a) Topography scan of the same area as in Figure S3 (80 pA, -1 V). **(b)** Spatial dependent of Dirac band gap modulation at B=0 T (-0.17V, 400 pA). **(c)** Dirac band gap map taken at 1 T field (-0.17 V, 400 pA) where gapped regions now form pattern (blue). **(d)** d*I*/d*V* spectra taken from the green circle in **(a)** at B=0 T (blue) and 1T (red). An exchange gap is opened in 1 T field where exchange coupling is enhanced by the external field. **(e)** Band gap histogram extracted from **(b)** which shows significant counts from gapless regions (dark red in **b**). **(f)** Histogram extracted from **(c)** which shows that Dirac band gaps are increased with a drastic decrease of gapless regions.

Figure S13 shows magnetic field dependent Dirac band gap maps from a region with a large concentration of Bi_{Mn} defects. Clearly, upon applying a perpendicular magnetic field of 1 T, the band gap map shows up more regions with small band gap around 10 meV. In some regions the band gap has increased from gapless to moderate value of 40 meV. As shown in **(f)**, there is now visible counts from regions with gap larger than 30 meV. Statistical analysis on the maps in **(b)** and **(c)** shows an increase of average band gap value from 4.6 meV to 14.8 meV. The emerging counts from moderate band gap region results in an increase of standard deviation from 12.5 meV to 18.3 meV and similar to the results in **Figure 4**, the restoration of Dirac band gap is accompanied by decreasing skewness from 4.5 to 1.5. The results in **Figure S13** indicates that regions with large numbers of Bi_{Mn} defects are typically much more gapless and the exchange gap can be restored partially with a perpendicular magnetic field of 1 T. Because Bi_{Mn} defects are non-magnetic, the pattern emerged in **Figure S13c** reflects the change of magnetic disorder in the center Mn^{2+} layer. The amount of Bi_{Mn} defects (see **Figure S3c**) could be responsible for the magnetic disorder.